

Key Points:

- Float data, linear theory, and a 3D model reveal vorticity and divergence control on inertial pumping beneath a fast-moving tropical cyclone
- Rightward-enhanced sea surface cooling of 1.2°C was dominated by mixing and modulated by rainfall, which suppressed cold water entrainment
- Estimates of turbulent diffusivity explain sea surface cooling rates 0.1°C hr<sup>-1</sup> under the tropical cyclone eye and thermocline mixing in its wake

Correspondence to:

N. G. Brizuela,  
nogutier@ucsd.edu

Citation:

Brizuela, N. G., Johnston, T. M. S., Alford, M. H., Asselin, O., Rudnick, D. L., Moum, J. N., et al. (2023). A vorticity-divergence view of internal wave generation by a fast-moving tropical cyclone: Insights from Super Typhoon Mangkhut. *Journal of Geophysical Research: Oceans*, 128, e2022JC019400. <https://doi.org/10.1029/2022JC019400>

Received 20 OCT 2022

Accepted 4 MAY 2023

Author Contributions:

**Conceptualization:** Noel G. Brizuela, T. M. Shaun Johnston, Matthew H. Alford, Olivier Asselin, James N. Moum

**Data curation:** T. M. Shaun Johnston, Daniel L. Rudnick, Elizabeth J. Thompson

**Formal analysis:** Noel G. Brizuela, Olivier Asselin, James N. Moum, Shuguang Wang, Chia-Ying Lee

**Funding acquisition:** T. M. Shaun Johnston, Matthew H. Alford, Daniel L. Rudnick, James N. Moum

**Investigation:** Olivier Asselin, James N. Moum, Shuguang Wang, Chia-Ying Lee

**Methodology:** Noel G. Brizuela, T. M. Shaun Johnston, Daniel L. Rudnick, Elizabeth J. Thompson, Shuguang Wang, Chia-Ying Lee

# A Vorticity-Divergence View of Internal Wave Generation by a Fast-Moving Tropical Cyclone: Insights From Super Typhoon Mangkhut

Noel G. Brizuela<sup>1</sup> , T. M. Shaun Johnston<sup>1</sup> , Matthew H. Alford<sup>1</sup> , Olivier Asselin<sup>2</sup> , Daniel L. Rudnick<sup>1</sup> , James N. Moum<sup>3</sup> , Elizabeth J. Thompson<sup>4</sup> , Shuguang Wang<sup>5</sup> , and Chia-Ying Lee<sup>6</sup>

<sup>1</sup>Scripps Institution of Oceanography, University of California, San Diego, La Jolla, CA, USA, <sup>2</sup>Ouranos, Montreal, QC, Canada, <sup>3</sup>College of Earth, Ocean and Atmospheric Science, Oregon State University, Corvallis, OR, USA, <sup>4</sup>NOAA Physical Sciences Laboratory, Boulder, CO, USA, <sup>5</sup>School of Atmospheric Sciences, Nanjing University, Nanjing, China, <sup>6</sup>Lamont-Doherty Earth Observatory, Columbia University, New York, NY, USA

**Abstract** Tropical cyclones (TCs) are powered by heat fluxes across the air-sea interface, which are in turn influenced by subsurface physical processes that can modulate storm intensity. Here, we use data from 6 profiling floats to recreate 3D fields of temperature ( $T$ ), salinity ( $S$ ), and velocity around the fast-moving Super Typhoon Mangkhut (western North Pacific, September 2018). Observational estimates of vorticity ( $\zeta$ ) and divergence ( $\Gamma$ ) agree with output from a 3D coupled model, while their relation to vertical velocities is explained by a linear theoretical statement of inertial pumping. Under this framework, inertial pumping is described as a linear coupling between  $\zeta$  and  $\Gamma$ , whose oscillations in quadrature cause periodic displacements in the ocean thermocline and generate near-inertial waves (NIWs). Vertical profiles of  $T$  and  $S$  show gradual mixing of the upper ocean with diffusivities as high as  $\kappa \sim 10^{-1} \text{ m}^2 \text{ s}^{-1}$ , which caused an asymmetric cold wake of sea surface temperature (SST). We estimate that  $\sim 10\%$  of the energy used by mixing was used to mix rainfall, therefore inhibiting SST cooling. Lastly, watermass transformation analyses suggest that  $\kappa > 3 \times 10^{-3} \text{ m}^2 \text{ s}^{-1}$  above  $\sim 110 \text{ m}$  depth and up to 600 km behind the TC. These analyses provide an observational summary of the ocean response to fast-moving TCs, demonstrate some advantages of  $\zeta$  and  $\Gamma$  for the study of internal wave fields, and provide conceptual clarity on the mechanisms that lead to NIW generation by winds.

**Plain Language Summary** Near-inertial internal waves (NIWs) are generated by winds and lead to oscillations in the internal structure of ocean currents and stratification. Turbulence induced by the vertical current shear in these waves helps sustain the upper ocean stratification and circulation. In this study, we use data from six autonomous floats deployed ahead of Super Typhoon Mangkhut to reconstruct the ocean's 3D response and compare it to output from a coupled air-sea model. Patterns in NIW are explained using simple linear equations based on vorticity and divergence rather than current velocities, providing an alternative view of how TC winds help generate waves in the stratified ocean interior. Measurements of temperature and salinity detail how turbulence mixed rainfall and thermocline waters into the upper ocean. Our analyses indicate that turbulent mixing rates are greatest within 100 km of the typhoon eye but remain elevated hundreds of kilometers in the TC wake. Theory and observations presented here provide a comprehensive view of the ocean response to fast-moving tropical cyclones.

## 1. Introduction

Tropical cyclones (TCs) power upper ocean currents that help redistribute heat and momentum throughout the water column (Geisler, 1970; Shay et al., 1989) and lead to turbulence that mixes thermal gradients, thereby exposing subsurface waters to atmospheric influence (Balaguru et al., 2012; Price, 1981). These processes are known to impact short-term weather forecasts (Schade & Emanuel, 1999) but may also cause variations in long-term climate (Emanuel, 2001; Fedorov et al., 2010). Furthermore, phytoplankton blooms behind TCs are thought to contribute as much as 20% of primary productivity in some marginal seas (Menkes et al., 2016). Therefore, untangling the multiple processes that unfold beneath and behind TCs is important to refine their representation in numerical weather prediction models, but also to understand the complex role of TCs in the Earth system.

**Project Administration:** T. M. Shaun Johnston, Daniel L. Rudnick, James N. Moum

**Resources:** Matthew H. Alford, Elizabeth J. Thompson, Shuguang Wang, Chia-Ying Lee

**Software:** Noel G. Brizuela, Matthew H. Alford, Shuguang Wang, Chia-Ying Lee

**Supervision:** T. M. Shaun Johnston, Matthew H. Alford

**Validation:** T. M. Shaun Johnston, Matthew H. Alford, Daniel L. Rudnick, Elizabeth J. Thompson

**Visualization:** Noel G. Brizuela

**Writing – original draft:** Noel G. Brizuela

**Writing – review & editing:** Matthew H. Alford, Olivier Asselin, James N. Moum, Elizabeth J. Thompson, Shuguang Wang

Near-surface currents that rotate near the inertial frequency ( $f$ ) dominate upper ocean dynamics behind fast-moving TCs (Geisler, 1970; Price, 1983; Shay et al., 1998). Transient winds amplify inertial currents on the right (left) side of Northern (Southern) hemisphere TCs but suppress them on the opposite side, thus causing an asymmetric distributing energy across TC tracks (Chang & Anthes, 1978; Price, 1981). Horizontal convergence and divergence associated with these currents lead to inertial pumping of the mixed layer (ML) base, which allows near-inertial internal waves (NIWs) to propagate down across the ML base and transfer momentum into the thermocline (Gill, 1984; Price, 1983). Although inertial pumping and its interactions with background ocean motions are beginning to be better understood (Balmforth et al., 1998; Kunze & Sanford, 1984; Sanford et al., 2021; Thomas et al., 2020; Whitt & Thomas, 2015), general approaches that help understand links between storm morphology and resulting patterns of NIW generation are still lacking.

Turbulence and advection associated with wind-driven currents help redistribute heat across subsurface reservoirs. Notably, shear-driven turbulence at the ML base cools the sea surface temperature (SST) during and shortly after TC passage, reducing subsequent heat fluxes to the atmosphere and helping modulate the intensity of TCs (Emanuel, 1999; Glenn et al., 2016). Without in-situ measurements of the turbulent diffusivity ( $\kappa$ ), only numerical models can isolate changes in stratification caused by mixing from the effects of upwelling and air-sea fluxes (Vincent et al., 2012; Zhang et al., 2018), but such models rely on imperfect parameterizations to represent mixing. Furthermore, better constraints on the magnitude and spatiotemporal extent of enhanced  $\kappa$  induced by TCs are crucial to understand and quantify the TC contribution to global ocean heat uptake and transport (Gutiérrez Brizuela et al., 2023).

In this article, we use data from six profiling floats (Johnston et al., 2020; Johnston & Rudnick, 2021) to reconstruct the 3D fields of temperature ( $T$ ), salinity ( $S$ ), and currents ( $u$ ,  $v$ ,  $w$ ) beneath Super Typhoon Mangkhut (Figure 1). Data are compared with output from a coupled 3D ocean-atmosphere model of Mangkhut (Johnston et al., 2021; Wang, 2020). Under the assumption that the upper ocean response to TC forcing approaches a steady state when viewed in storm-following coordinates (Geisler, 1970), we diagnose the roles of upwelling, advection, and mixing in the redistribution of subsurface heat and rainfall inputs. Float velocity data are used to validate linear theory results showing that upwelling and NIW generation under TCs result from the coupling of ML vorticity ( $\zeta \equiv \frac{\partial v}{\partial x} - \frac{\partial u}{\partial y}$ ) and divergence ( $\Gamma \equiv \frac{\partial u}{\partial x} + \frac{\partial v}{\partial y}$ ) by Earth's rotation. As explained below, this coupling is equivalent to the horizontal rotation of near-inertial currents under TCs as examined by Geisler (1970); Price (1983), and others. As argued below, changing variables to vorticity and divergence provides additional insight on the mechanisms of upwelling and NIW generation under TCs.

Section 2 describes our data and processing methods including details about the 3D model used for validation. Section 3 lays out the linear theory of upwelling and NIW generation under TCs and reformulates standard ML dynamics in terms of  $\zeta$  and  $\Gamma$  to demonstrate their inertial coupling. Section 4 presents observational and modeled maps of ( $u$ ,  $v$ ) to verify relations between wind forcing, vorticity, divergence and NIW generation. Indirect evidence of turbulent mixing under Mangkhut is presented using float measurements of  $T$  and  $S$  in Section 5. A discussion of our methods and results is presented in Section 6, while conclusions are given in Section 7.

## 2. Data and Methods

### 2.1. Data Collection

Super Typhoon Mangkhut originated on 7 September 2018 as a tropical depression in the central Pacific Ocean and later intensified as it moved westwards into the Philippine Sea. Between 11 and 15 September, when our measurements were made, Mangkhut always sustained maximum 1-min wind speeds between 70 and 80 m s<sup>-1</sup> (Figure 1b), equivalent to a category 5 hurricane. Between 11 and 14 September, Mangkhut's mean translation speed was approximately  $U_{storm} \approx 6.2$  m s<sup>-1</sup> or twice the local group speed ( $c_g$ ) of the first baroclinic mode, making it a fast-moving TC whose ocean response was dominated by NIWs (Geisler, 1970; Nilsson, 1995). Throughout the TC's period of maximum intensity, SOLO-II floats (Davis et al., 2001) sampled the ocean response under the TC (Figure 1b). The combination of Mangkhut's long lifespan and elevated intensity put it among the 0.5% most powerful tropical storms on record (Figure 1c, Emanuel, 2005). As it traveled through the Philippine and South China Seas, Mangkhut caused significant damage and loss of life in the Philippines, Guam, Taiwan, Hong Kong, and China (Wamsley, 2018).

Upon deployment, the floats modified their buoyancy to dive up to 200 m depth and back to the surface at intervals <50 min. While doing so, they obtained upward profiles of  $T$  and  $S$ , and drifted westward with the

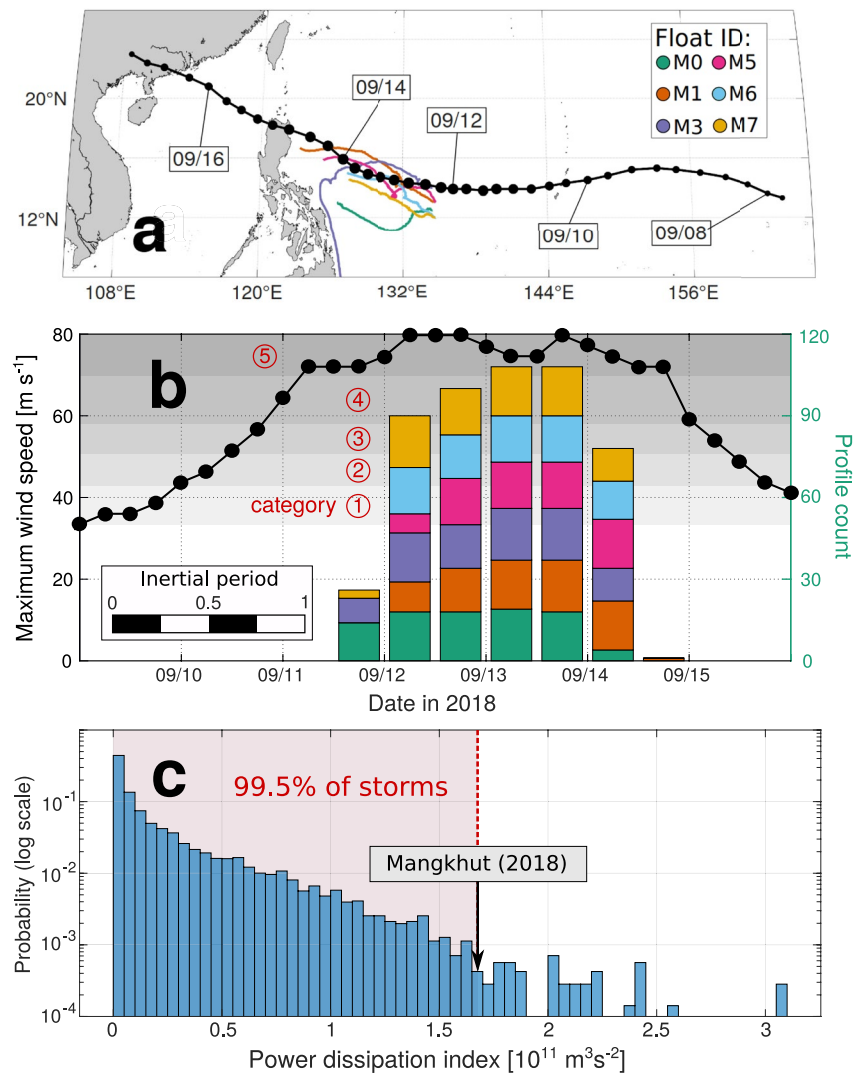


**Figure 1.** Tropical cyclone (TC) overview. (a) Best track data (Joint Typhoon Warning Center, 2022) shown in black and float trajectories are in colors. (b) Maximum 1-min sustained wind speed  $|U_{10}|$  (dotted line, left axis) and histogram showing the time distribution of float measurements. Gray shading in (b) shows the wind speed thresholds for Saffir-Simpson TC categories 1 ( $\|U_{10}\| \leq 30 \text{ m s}^{-1}$ ) to 5 ( $|U_{10}| > 70 \text{ m s}^{-1}$ ). (c) Probability distribution of power dissipation index estimated for  $>7,000$  storms puts Mangkhut among the 0.5% most powerful tropical storms in record.

North-Equatorial Current at  $\sim 0.18 \text{ m s}^{-1}$  (Figure 2a, Johnston et al., 2020). Because floats record their coordinates at the beginning and end of every dive cycle, their Global Positioning System data yields two estimates of horizontal velocity (Figure 2b).  $\mathbf{u}_{mean}$  is the depth-mean current over the profiling range and is calculated using the difference between the start and end locations of individual dives. Surface estimates  $\mathbf{u}_{surf}$  which are subject to wave motion and windage, are calculated using the drift between consecutive dives, when floats remain at the surface for  $\sim 5$  min while they transfer data via Iridium satellite.

Output from a coupled ocean-atmosphere model of Mangkhut is compared to dynamical insights derived from float velocity data. The coupled system uses the Weather Research and Forecast (WRF) model V3.8.1 (Skamarock et al., 2008) as its atmospheric component, while the ocean is represented by the Hybrid Coordinate Ocean Model V2.2 (HYCOM; Wallcraft et al., 2009). Horizontal grid spacing in HYCOM was  $1^\circ/12^\circ$  for 41 vertical layers (10 in the upper 50 m) and output was saved at 3 hr intervals. Chen and Curcic (2016) give an assessment of this coupled model's performance under North Atlantic TCs. Further details about the model configuration used for Mangkhut were given by Johnston et al. (2021).

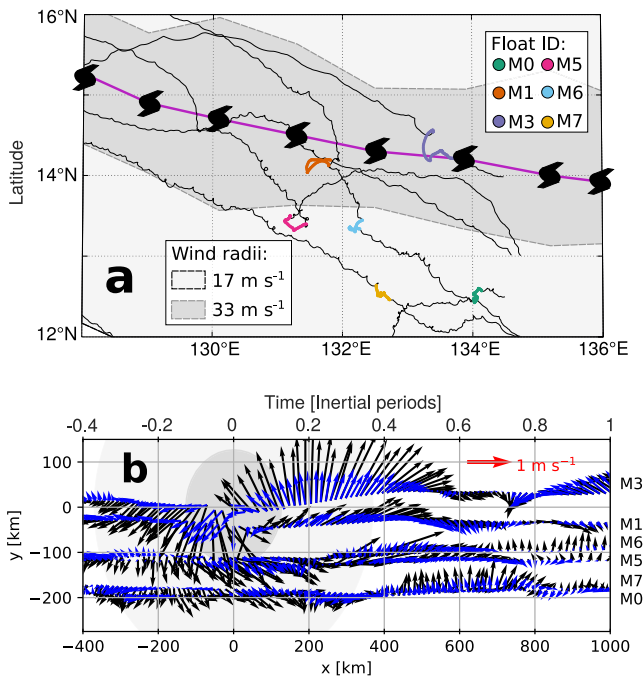


**Figure 2.** (a) 6-hr best track data for Mangkhut (black vortices). Black lines mark float trajectories, while the locations of vertical profiles used in this study are highlighted in colors. (b) Plane view of  $\mathbf{u}_{surf}$  (black) and  $\mathbf{u}_{mean}$  (blue), with  $x$  and  $y$  components scaled equally to show the true direction of currents in storm-following coordinates ( $x, y$ ).

Despite the fact that each float effectively sampled different parts of the storm at different times (Figure 2a), both  $\mathbf{u}_{surf}$  and  $\mathbf{u}_{mean}$  line up with  $v < 0$  ( $v > 0$ ) for  $x < 0$  ( $x > 0$ ) and later rotate in the clockwise sense in the TC wake. Such similarities in measurements made by different floats at different times in Figure 2b suggest that the ocean response was steady within the TC-following ( $x, y$ ) coordinates (Geisler, 1970). To best exploit the spatiotemporal information embedded in float data, we used objective mapping (Davis, 1985; Le Traon et al., 1998) with a Gaussian decorrelation scale of 150 km to horizontally interpolate measurements  $\mathbf{u}_{surf}$ ,  $\mathbf{u}_{mean}$ ,  $T$ , and  $S$ . The signal-to-noise ratio for objective mapping was set to 10, and areas where the estimated mean square error of interpolated fields is greater than 7.5% of signal variance have been masked out in plots.

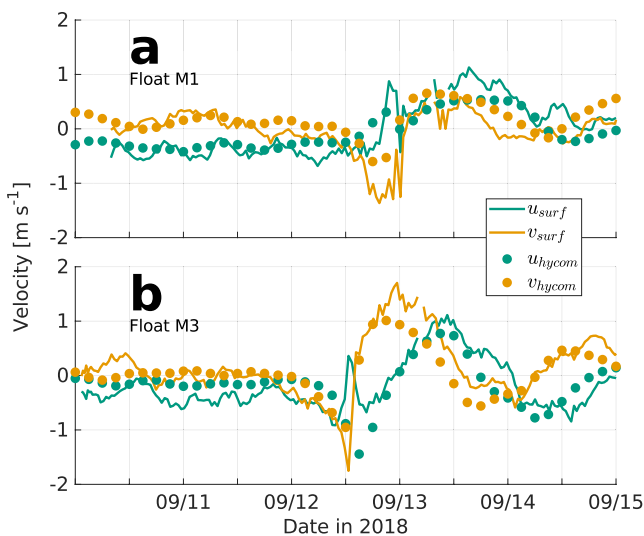


**Figure 3.** Model-observation comparison of upper ocean velocities. Mixed layer (ML) velocities  $\mathbf{u}_{hycom}$  (circles) at fixed locations in the coupled 3D model are compared against measurements  $\mathbf{u}_{surf}$  (solid lines) from floats (a) M1 and (b) M3.

Comparisons of model output against measured  $\mathbf{u}_{surf}$  (Figure 3) are indicative of both the accuracy of the simulation and that of float velocity estimates. Although qualitative agreement between both datasets is good, neither float nor model data in Figure 3 should be regarded as ground truth for ocean conditions at a time and place. While  $\mathbf{u}_{surf}$  may be biased by windage or wave motion, the model's atmospheric component lets Mangkhut evolve dynamically, such that the modeled track and intensity differ slightly from observations (Johnston et al., 2021). To account for this, model velocities  $\mathbf{u}_{hycom}$  in Figure 3 were taken from the average location of each float within 24 hr of TC passage. As described next, objective mapping of float data onto storm-following coordinates provides a more meaningful representation of ML dynamics under Mangkhut than pointwise comparisons in Figure 3.

## 2.2. 3D Reconstruction of the Ocean Response

Best track data for Mangkhut (Joint Typhoon Warning Center, 2022) was linearly interpolated to the times of float data, which were then reorganized in storm-following coordinates ( $x, y$ ) (Figure 2b). Positive values of  $x$  denote regions behind the storm eye, while  $y > 0$  indicates locations right of the TC track. Likewise,  $\mathbf{u}_{surf}$  and  $\mathbf{u}_{mean}$  were rotated such that  $u$  and  $v$  represent along-track and cross-track velocities respectively. Plots in ( $x, y$ ) use the equivalent time  $t = x/U_{storm}$  to preserve information about temporal variability that has been mapped onto  $x$ . We use  $U_{storm} = 6.2 \text{ m s}^{-1}$  to characterize Mangkhut between September 11 and 14, when its translation speed remained nearly constant (RMSE  $0.5 \text{ m s}^{-1}$ ) and  $\sim 85\%$  of our measurements were made (Figure 1b). Time scaling  $t \frac{L}{2\pi}$  used in visualizations uses the inertial period  $\frac{2\pi}{f}$  at  $15.54^\circ\text{N}$  ( $\sim 45 \text{ hr}$ ) such that one inertial period in  $t$  corresponds to  $U_{storm} \frac{2\pi}{f} = 1,000 \text{ km}$  in  $x$  (Figure 2b).

To reconstruct 3D patterns in  $T$  and  $S$ , we stacked 2D maps at 5 m intervals, thus producing  $T^*(x, y, z)$  and  $S^*(x, y, z)$ . Here, the star \* denotes objectively mapped variables. Although vertical variations in  $u, v$  were not measured directly, we use differences between  $\mathbf{u}_{surf}^*$  and  $\mathbf{u}_{mean}^*$  to separate the ML flow from the less energetic ocean below (Johnston et al., 2021). More precisely, we assume that depth-dependence at each location ( $x, y$ ) is given by

$$\mathbf{u}^*(x, y, z) = \begin{cases} \mathbf{u}_{surf}^* & z \geq -h \\ \mathbf{u}_{surf}^* + \left\langle \frac{\partial \mathbf{u}}{\partial z} \right\rangle (z - h) & -h > z > -h - l \\ \mathbf{u}_{surf}^* + \left\langle \frac{\partial \mathbf{u}}{\partial z} \right\rangle l & -h - l \geq z \geq -H. \end{cases} \quad (1)$$

The piecewise function (Equation 1) includes two layers of depth-constant velocity and a sheared transition layer between them. Flow in the uppermost layer, which spans the depth of the ML  $-h < z \leq 0$ , is given by  $\mathbf{u}_{surf}^*$ . Here,

$h$  is defined as the depth at which  $T^*$  is  $0.2^\circ\text{C}$  colder than it is at 20 m depth; this helps avoid transient effects of diurnal warm layers and rain layers, whose timescale of dynamical significance under intense wind forcing is much shorter than that of near-inertial motions (E. J. Thompson et al., 2019; Hughes et al., 2020). Below  $z = -h$ , we assume a transition layer of thickness  $l$  and constant shear

$$\left\langle \frac{\partial \mathbf{u}}{\partial z} \right\rangle = 2H \frac{\mathbf{u}_{surf}^* - \mathbf{u}_{mean}^*}{[l^2 + 2l(H - l - h)]}. \quad (2)$$

This transition layer is set by the vertical penetration of wind-driven turbulent momentum, which determines the depth at which  $\mathbf{u}$  no longer behaves like a slab (Pollard et al., 1973; Turner & Kraus, 1967). In reality, the transition layer thickness can vary considerably and is seen as a stratification and shear maximum below the ML base (Johnston & Rudnick, 2009). However, vigorous mixing and internal wave strain behind Mangkhut makes it such that a transition layer cannot be reliably identified in profiles of  $T$  and  $S$  at many locations. Therefore, we set a constant thickness  $l = 30$  m, which is based on the mean value found by Johnston and Rudnick (2009) when defining the transition layer based on the magnitude of the vertical shear squared. Lastly, the third and deepest layer extends down to  $H = 180$  m and has velocities  $\mathbf{u}_{surf}^* + \left\langle \frac{\partial \mathbf{u}}{\partial z} \right\rangle l$ . Here,  $H$  is set by the depth of individual float dives, which ranged between 180 and 200 m. This way, Equations 1 and 2 force the depth-mean of  $\mathbf{u}^*$  between  $z = 0$  and  $z = -H$  to be equal to  $\mathbf{u}_{mean}^*$ .

Concentrating  $\left\langle \frac{\partial \mathbf{u}}{\partial z} \right\rangle$  within a transition layer captures some of the main features of wind-forced currents. Thus, Equations 1 and 2 yield an idealized 3D velocity field constrained by float velocity estimates and previous knowledge of the baroclinic response to TC forcing. However, it should be noted that high baroclinic modes that cannot be represented by Equation 1.

To finalize the reconstruction of 3D flows beneath Mangkhut from float measurements, we impose a condition of adiabatic continuity to obtain  $\frac{\partial w^*}{\partial z} = -\frac{\partial u^*}{\partial x} - \frac{\partial v^*}{\partial y}$ . Furthermore, we assume a rigid lid so that  $w^*(z = 0)$  vanishes and the vertical velocity is

$$w^*(x, y, z) = \int_0^z \left( \frac{\partial u^*}{\partial x} + \frac{\partial v^*}{\partial y} \right) dz'. \quad (3)$$

Before showing the interpolated fields  $T^*$ ,  $S^*$ ,  $u^*$ ,  $v^*$ ,  $w^*$ , we must emphasize that (a) they only resolve gradients at scales  $\sim 150$  km and greater, given the decorrelation lengthscale  $L = 150$  km and the maximum float separation of roughly 100 km. Moreover, (b) Caution is warranted when interpreting results near the edge of the objective maps, and (c) while Equation 1 loosely approximates the vertical structure of a mode 1 baroclinic mode, the full ocean response to TC winds includes higher vertical modes that drive shear throughout the thermocline (Shay et al., 1989, 1998). Therefore,  $w^*$  can reproduce vertical displacements at the ML base but may fail to capture realistic variations deeper in the water column.

### 2.3. Thorpe Scale Estimates of Turbulence

Vertical profiles of  $T$  and  $S$  taken at 1 Hz (vertical resolution  $\sim 0.2$  m) were used to compute in situ density ( $\rho$ ). These allowed us to derive Thorpe scale estimates (Thorpe, 1977) of the turbulent dissipation rate ( $\varepsilon$ ) and diffusivity ( $\kappa$ ) within unstable overturns where  $\frac{\partial \rho}{\partial z} > 0$ . This method relies on reordering vertical profiles of  $\rho$  to obtain  $\rho_{\text{ordered}}$  such that  $\frac{\partial \rho_{\text{ordered}}}{\partial z} \leq 0$ ; then, an overturn is said to span every contiguous vertical range for which  $\rho \neq \rho_{\text{ordered}}$ . For each overturn, we compute the set of vertical displacements  $d'$  necessary to turn  $\rho$  into  $\rho_{\text{ordered}}$  and viceversa, thus defining the Thorpe scale as  $L_{Ti} = \sqrt{\langle d'^2 \rangle_i}$ , where the brackets indicate averaging within an overturn  $i$ . Given this,  $\varepsilon$  was calculated as

$$\varepsilon_i = 0.64 L_{Ti}^2 \langle N \rangle_i^3. \quad (4)$$

Here,  $\langle N \rangle_i$  is the mean buoyancy frequency calculated from the sorted profile of  $\rho$ . To filter out spurious overturns caused by random noise and spikes in our data, estimates of  $\varepsilon$  were discarded for overturns in which any of the following were true.

1. The height of overturning cells ( $D_z$ ) was less than 5 m (this choice was made for consistency, as 5 m is the vertical resolution of  $T^*$  and  $S^*$ ).

2.  $D_z < 2\Delta\rho_{\text{noise}} \left\langle -\frac{\partial\rho}{\partial z} \right\rangle_i^{-1}$ , where  $\Delta\rho_{\text{noise}} = 5 \times 10^{-4} \text{ kg m}^{-3}$  is the standard error in  $\rho$  data (Galbraith & Kelley, 1996).
3. The change in density across an overturn is less than  $2\Delta\rho_{\text{noise}}$
4. Positive displacements ( $d' > 0$ ) make up less than 20% or more than 80% of all  $d'$  values within the overturning cell (Gargett & Garner, 2008).

Next, valid estimates of  $\varepsilon$  were used with the relation in Osborn (1980) to compute  $\kappa_i = 0.2 \frac{\varepsilon_i}{N^2}$ . Here,  $\tilde{N}$  is the background buoyancy frequency from sorted profiles of  $\rho$ . This allows us to estimate the downward turbulent heat flux

$$J_{qi} = \rho_0 C_p \kappa_i \left\langle \frac{\partial T}{\partial z} \right\rangle_i \quad (5)$$

Here, the constants are  $\rho_0 = 1,024 \text{ kg m}^{-3}$  and  $C_p = 4000 \text{ J kg}^{-1}\text{C}^{-1}$ . Comparisons between Thorpe-inferred quantities and microstructure measurements suggest that Equation 4 can yield valid estimates in the thermocline beneath a TC, where temperature gradients are sharp and convective instability is not the main driver of turbulence (Alford et al., 2006; Dillon, 1982; Dunckley et al., 2012; Ferron et al., 1998; Hamann et al., 2021; Mater et al., 2015). More details on the implementation, assumptions, and limitations of the Thorpe scale method can be found in Johnson and Garrett (2004), A. Thompson et al. (2007), and Scotti (2015) and references therein.

### 3. Mixed Layer Theory

In this section, we review the mechanisms of NIW generation by TCs and formulate the relevant linear ML dynamics. Instead of understanding ML motions using depth-averaged ML currents  $\bar{\mathbf{u}} = (\bar{u}, \bar{v})$ , we use their vorticity ( $\zeta = \mathbf{k} \cdot \nabla \times \bar{\mathbf{u}}$ ) and divergence ( $\Gamma = \nabla \cdot \bar{\mathbf{u}}$ ). This change of variables leads to a coupling between  $\zeta$  and  $\Gamma$  that gives rise to inertial pumping and helps conceptualize NIW generation by TCs as a 1D rather than 3D process. By stating inertial pumping as a set of ordinary differential equations rather than partial differential equations, as done by Gill (1984), the spatiotemporal patterns of NIW generation are more easily related to the morphology of atmospheric forcing  $\tau = (\tau_x, \tau_y)$ . In order to simplify the notation, the projection onto the vertical unit vector  $\mathbf{k}$  is henceforth implied when computing the curl of 2D vector fields.

The response of  $\bar{\mathbf{u}}$  to  $\tau$  in a ML of thickness  $h$  can be described using the linear slab model

$$\frac{\partial \bar{u}}{\partial t} = f \bar{v} + \frac{\tau_x}{\rho_0 h} - r \bar{u} \quad (6)$$

$$\frac{\partial \bar{v}}{\partial t} = -f \bar{u} + \frac{\tau_y}{\rho_0 h} - r \bar{v} \quad (7)$$

$$\frac{\partial h}{\partial t} + h \nabla \cdot \bar{\mathbf{u}} = W_e. \quad (8)$$

Pollard and Millard (1970) first used these equations to explain in situ measurements of  $\bar{\mathbf{u}}$ , while recent studies have shown their skill in reproducing the ocean response to TCs (Guan et al., 2014). Solutions to Equations 6 and 7 may be written as the sum of two terms (D'Asaro, 1985), one that varies slowly and approximates an Ekman balance, and another representing near-inertial oscillations whose amplitude decays exponentially due to the damping coefficient  $r$ . In order to resolve vertical velocities at the ML base  $\left(\frac{\partial h}{\partial t}\right)$ , we couple Equations 6 and 7 to the continuity Equation 8. Here,  $W_e \geq 0$  is an entrainment rate used to represent ML deepening caused by turbulent mixing (Price, 1981).

Because our focus here is on NIW generation, Equations 6–8 exclude pressure gradient and advection terms that make negligible or secondary contributions to  $\frac{\partial h}{\partial t}$  under TCs. Even though horizontal surface pressure gradients drive flows in TC wakes (Shay & Chang, 1997), they scale to make a negligible contribution to  $\frac{\partial h}{\partial t}$  (D'Asaro, 1989; Geisler, 1970; Gill, 1984). Similarly, nonlinear solutions of  $\frac{\partial h}{\partial t}$  by Price (1981) are in agreement with linear analytical results obtained for fast-moving storms Geisler (1970), suggesting that the advective terms can be dropped from the equations of motion (Figure 10 in Price, 1981). While 3D effects associated with the pressure and advection terms may play a significant role under slow-moving TCs (Yablonsky & Ginis, 2009), simplified dynamics in Equations 6–8 can reproduce the ocean response to fast-moving TCs, defined as those whose translation speed  $U_{\text{storm}}$  is greater than the local group speed ( $\mathbf{c}_g$ ) of the first baroclinic mode ( $U_{\text{storm}}/\mathbf{c}_g > 1$ ) (Geisler, 1970; Nilsson, 1995).

When the ML base oscillates at frequencies slightly greater than  $f$ , periodic pumping of the ML base and pressure gradients that result under it allow downward momentum transfer in the form of NIWs (Gill, 1984; Price, 1983). Therefore, the full baroclinic ocean response to TCs must be represented by coupling contiguous layers of increasing density through interfacial displacements (Geisler, 1970; Price, 1983). Given that their focus is on the ML, Equations 6 and 7 do not represent these thermocline processes explicitly. Rather, they use the empirical damping rate  $r$  to parameterize the gradual decay of ML momentum that results from internal wave propagation, nonlinearities, and turbulent dissipation (D'Asaro, 1989; D'Asaro et al., 1995; Pollard & Millard, 1970; ).

The value of  $r$  is typically determined empirically to fit observations of  $\bar{\mathbf{u}}$ , which can yield timescales  $r^{-1}$  that range from 8 hr to eight or more days (Alford & Gregg, 2001; Guan et al., 2014; Pollard & Millard, 1970). This broad range may be due to the fact that  $r$  is meant to represent the effects of all dynamics ignored in Equations 6 and 7. Previous studies have sought to derive scalings of the type  $r^{-1} \sim E_{NIW}/F_{NIW}$ , where  $E_{NIW}$  is the near-inertial energy and  $F_{NIW}$  is the corresponding energy flux (Gill, 1984). However, such derivations are necessarily incomplete and depend on assumptions about the physical process by which NIWs develop horizontal gradients and their corresponding group velocity ( $\mathbf{c}_g$ ). In the mid latitudes, this reduction of horizontal scales is thought to depend on gradients in the mesoscale and planetary vorticity (Asselin & Young, 2020; D'Asaro, 1989; Johnston et al., 2016; Kunze, 1985; Thomas et al., 2020), while the spatial structure of TC winds imprints sharp gradients on upper ocean currents and thus allows for more rapid generation of NIWs (D'Asaro, 1989). To emphasize this feature of NIW generation by TCs, we now consider the ML response to  $\tau$  in terms of  $\bar{u}$  and  $\bar{v}$ , but their spatial gradients. The final aim here is to elucidate the drivers of inertial pumping in  $\frac{\partial h}{\partial t}$ , by which NIW energy propagates into the thermocline.

### 3.1. Dynamics of Wind-Forced Gradients in the Upper Ocean

Below, we manipulate Equations 6–8 to isolate the components that contribute to  $\frac{\partial h}{\partial t}$  and thus generate NIWs. To do this, we calculate  $\frac{\partial \zeta}{\partial t} = \nabla \times \frac{\partial \bar{\mathbf{u}}}{\partial t}$  and study its relation to  $\frac{\partial \Gamma}{\partial t} = \nabla \cdot \frac{\partial \bar{\mathbf{u}}}{\partial t}$ . Taking the curl and divergence of Equations 6 and 7 thus yields an alternative representation of ML dynamics

$$\frac{\partial \zeta}{\partial t} = -f\Gamma + \frac{1}{\rho_0 h} \left( \nabla \times \tau - \frac{\tau}{h} \times \nabla h \right) - r\zeta \quad (9)$$

$$\frac{\partial \Gamma}{\partial t} = f\zeta + \frac{1}{\rho_0 h} \left( \nabla \cdot \tau - \frac{\tau}{h} \cdot \nabla h \right) - r\Gamma \quad (10)$$

$$\frac{\partial h}{\partial t} + h\Gamma = W_e. \quad (11)$$

This formalism does not explicitly include information about the magnitude and direction of currents. Instead, it uses the physical principles in Equations 6–8 to resolve spatiotemporal patterns in  $\frac{\partial h}{\partial t}$  that generate internal waves. While past studies have used  $\zeta$  and  $\Gamma$  as the basis of fluid dynamical models (Névir & Sommer, 2009; Salmon, 2007), these variables are particularly relevant to NIW generation and their interaction with background flows (Gill, 1984; Nagai et al., 2015; Whitt & Thomas, 2015). Furthermore, note that under axial-symmetric storms,  $\nabla \cdot \tau$  and  $\nabla \times \tau$  are fully determined by radial and tangential winds respectively. Thus, Equations 9 and 10 show how these separate components of  $\tau$  directly drive orthogonal but coupled modes of motion  $\Gamma$  and  $\zeta$  in the ML.

In TC wakes, once winds cease to play a dominant role and the ML evolves freely, our diagnostic model (Equations 9–11) yields the three term balance

$$\frac{\partial \zeta}{\partial t} = -f\Gamma - r\zeta \quad (12)$$

$$\frac{\partial \Gamma}{\partial t} = f\zeta - r\Gamma. \quad (13)$$

This linear system of equations, a damped harmonic oscillator, produces inertial cycles in  $\zeta$  and  $\Gamma$  with an exponential decay rate  $r$ . Inertial pumping arises directly from these cycles, which are simply a consequence of clockwise rotation in  $\bar{\mathbf{u}}$  over time at a given point in the TC wake. To visualize how Equations 12 and 13 are an explicit statement of inertial pumping, we follow Gill (1984) and set  $\tau = W_e = r = 0$  to consider an initial condition  $(\zeta_i, \Gamma_i) = (c_i, 0)$  at time  $t = t_i$ , where  $c_i > 0$ . As illustrated in Figure 4, Equations 12 and 13 imply that inertial rotation of current vectors transforms  $\zeta$  into  $\Gamma$  and  $\Gamma$  into  $-\zeta$  at time intervals  $\sim \frac{\pi}{2f}$ . Quadrature between  $\zeta$  and  $\Gamma$  in this

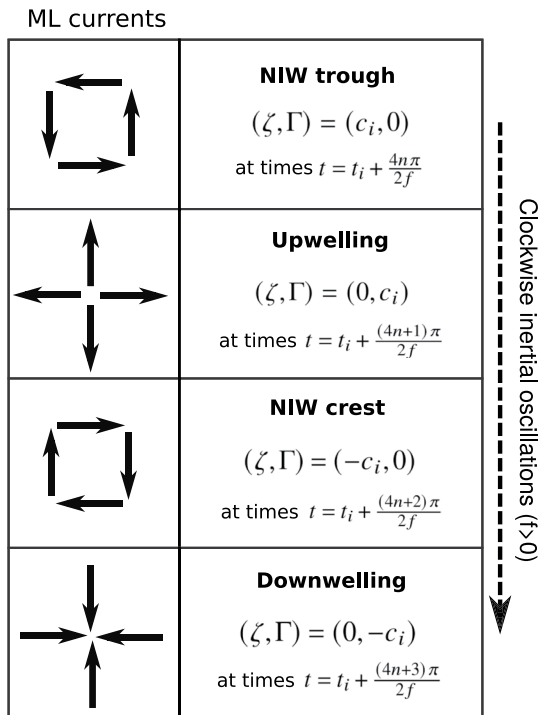


**Figure 4.** Successive rows illustrate the time evolution of current vectors under clockwise inertial oscillations. The left column shows schematic views of  $\mathbf{u}$  at temporal intervals  $\frac{\pi n}{2f}$  ( $n = 0, 1, 2, \dots$ ). Over this period, clockwise rotation of  $\mathbf{u}$  by  $90^\circ$  fully transforms  $\zeta$  into  $\Gamma$ , and  $\Gamma$  into  $-\zeta$ .

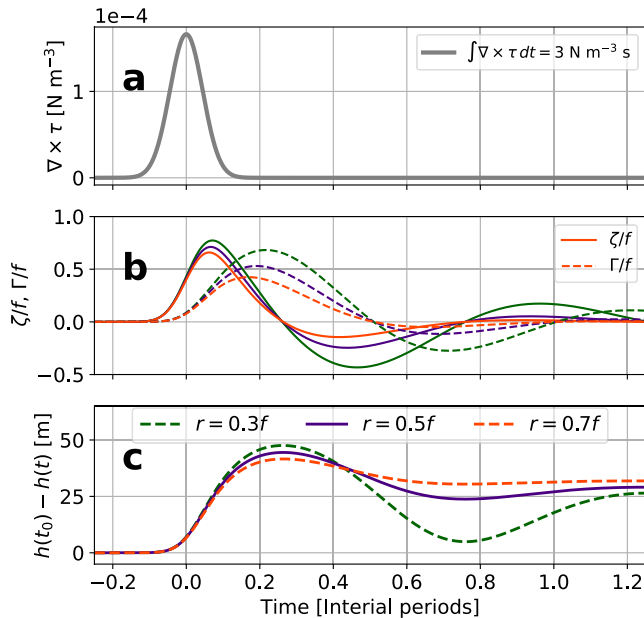


**Figure 5.** Mixed layer response Equations 9–11 to (a) wind vortex representing the radial wind stress of an axisymmetric tropical cyclone. (b) shows the evolution of  $\zeta/f$  (solid lines) and  $\Gamma/f$  (dashed lines) for damping parameters  $r = 0.3f$ ,  $0.5f$ , and  $0.7f$  in green, purple, and orange, respectively. (c) shows corresponding solutions of the mixed layer displacement  $h(t_0) - h(t)$  when  $W_e = 0$ .

oscillatory mode means that NIW crests and troughs (maximum upward and downward displacements of the ML base) must be surrounded by anticyclonic and cyclonic inertial currents respectively (Figure 4).

### 3.2. Relating Upwelling and NIW Generation to TC Winds

When winds act on the ocean surface,  $\bar{\mathbf{u}}$  initially accelerates in the direction of  $\tau$  while turbulence helps distribute momentum vertically and deepen the ML. Later on,  $\bar{\mathbf{u}}$  undergoes inertial rotation and becomes misaligned with  $\tau$ . Variations in the alignment between  $\tau$  and  $\bar{\mathbf{u}}$  play a crucial role in setting the ocean response to TCs, as misalignment gives rise to an asymmetric distribution of ML energy around the TC track (Chang & Anthes, 1978) and can stop ML deepening by turbulence when  $\bar{\mathbf{u}}$  approaches Ekman's balance and the rate of wind work  $\tau \cdot \bar{\mathbf{u}}$  vanishes (Ekman, 1905; Pollard et al., 1973).

Setting  $\nabla h = 0$  in Equations 9–11, we may write the Ekman balance as  $(\zeta, \Gamma) \sim \frac{1}{f\rho_0h}(-\nabla \cdot \tau, \nabla \times \tau)$ , so that  $\Gamma$  (and the resulting upwelling) is sustained by  $\nabla \times \tau$ . However, notice that  $\nabla \times \tau$  does not directly drive the evolution of  $\Gamma$  in Equation (10). Instead,  $\frac{\partial \zeta}{\partial t}$  and  $\frac{\partial \Gamma}{\partial t}$  will mirror patterns in  $\nabla \times \tau$  and  $\nabla \cdot \tau$  respectively at the initial stages of TC forcing. It is only later that the inertial rotation of currents gradually links  $\nabla \times \tau$  to  $\Gamma$  and produces upwelling (Figure 4).

The relative magnitude of steady (Ekman) and oscillating (NIWs) components of the ocean response to TC forcing is determined by  $U_{storm}/c_g$  and the horizontal scale of  $\tau$ . Using a two-layer model, Geisler (1970) showed that energy transfer into NIWs decreases with the ratio  $U_{storm}/c_g$ . At the limit where  $U_{storm}/c_g < 1$  (slow-moving TCs), Geisler's solutions predict that the momentum in  $\nabla \times \tau$  is entirely used by Ekman style upwelling with no oscillatory behavior. Nilsson (1995) later generalized this result by deriving analytical expressions for the power put into geostrophic and NIW modes in a continuously stratified fluid given  $c_g$ ,  $U_{storm}$ , and the wavenumber spectrum of  $\tau$ .

The formalism in Equations 9–11 does not explicitly represent  $c_g$ , but instead uses  $r$  to parameterize Eulerian momentum decay. Hence, we investigate how the value of  $r$  influences the relative roles of NIW generation and net upwelling as described by the  $(\zeta, \Gamma)$  slab model. To do this, we used Euler's method to compute point solutions (solving with no space dependence, such that  $\nabla h = 0$ ) of the slab model under the forcing of a Gaussian vortex  $\nabla \times \tau$  (Figure 5a). This represents the changing direction of tangential  $\tau$  inside an axisymmetric TC eye but does not include radial stresses  $\nabla \cdot \tau$ , which are known to make only minor contributions to NIW generation under TCs (Nilsson, 1995; Price, 1983; Shay et al., 1989). The evolution of  $(\zeta/f, \Gamma/f, h)$  from an initial condition  $(0, 0, 80 \text{ m})$  using  $f$  at  $15.5^\circ\text{N}$  and  $r \in [0.3f, 0.7f]$  is shown in Figures 5b and 5c.

Numerical solutions show that increasing the value of  $r$  weakens near-inertial oscillations in  $\zeta/f$ ,  $\Gamma/f$ , and  $h(t)$ , and enhances the net ML displacement  $h(t_0) - h(t)$  at long times (Figure 5). Namely, greater values of  $r$  produce an ocean response that is akin to that of storms with lower  $U_{storm}/c_g$ , as  $h(t_0) - h(t)$  continues to oscillate after its maximum displacement if  $r = 0.3f$ , but converges shortly after its peak when  $r = 0.7f$ . This suggests that the sensitivity of the  $(\zeta, \Gamma)$  slab model in Equations 9–11 to the damping parameter  $r$  is consistent with the notion developed around the  $(u, v)$  model that  $r$  is directly proportional to  $c_g$  and helps parameterize its effects. Namely, underlying ocean conditions impacting the partition of energy between geostrophic and NIW modes in TC wakes can be partly represented by tuning  $r$ .



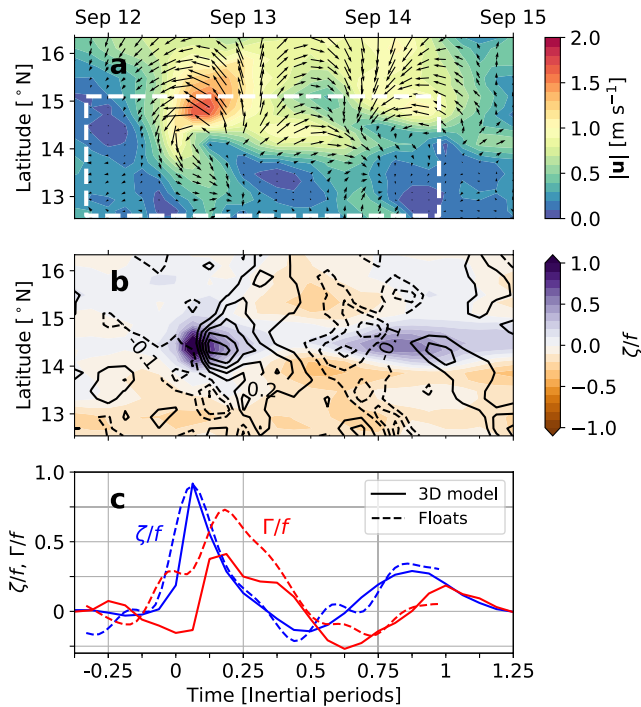


**Figure 6.** Hovmöller diagrams of the mixed layer flow along 133°E in terms of (a)  $\bar{u}$  and (b)  $(\zeta, \Gamma)/f$  from the 3D coupled model, where  $\Gamma/f$  is contoured at 0.1 intervals (dashed/solid for negative/positive values). (c) Modeled  $(\zeta, \Gamma)/f$  averaged between 14° and 14.5°N (solid lines) is compared to observed values along  $y = 0$  (dashed lines). The dashed rectangle in panel a is representative of the area and stages of ocean response sampled by floats (Figure 2b).

The linear  $(\zeta, \Gamma)$  view of ML dynamics in Equations 9–11 does not include any new physics absent from standard ocean models based on  $(u, v)$ . Rather, it uses a simple change of variables to explain inertial pumping (Figure 4) using ordinary differential equations instead of partial ones, as done by Gill (1984). This helps conceptualize inertial pumping and upwelling as 1D (rather than 3D) processes. Furthermore, coupling between  $\zeta$  and  $\Gamma$  concretely explains why NIW wakes are generally centered along the TC track where  $\nabla \times \tau$  peaks and not on its right side, where the greatest concentration of near-inertial energy is (Price, 1981, 1983). Namely, NIWs only form where horizontal gradients ( $\zeta$  and  $\Gamma$ ) exist, and the forcing  $\nabla \times \tau$  that directly drives cycles in  $\zeta$  and  $\Gamma$  is greatest along the track.

Overall, numerical solutions in Figure 5 show that Equations 9–11 can reproduce inertial pumping and upwelling under TCs but rely on tuning of the parameter  $r$ . Furthermore, note that the 1D approach used here does not include the effects of pressure gradients and horizontal advection, which may have greater relevance under slow-moving TCs ( $U_{storm}/c_g \leq 1$ ). In the next section, we use float measurements and output from WRF-HYCOM coupled simulations of Mangkhut ( $U_{storm}/c_g \sim 2$ ) to demonstrate the relevance of Equations 9–11 and  $(\zeta, \Gamma)$  coupling (Figure 4) in describing NIW generation under fast-moving TCs.

#### 4. Upper Ocean Dynamics Beneath Mangkhut

We now turn our attention toward model output and observations of upper ocean dynamics beneath Super Typhoon Mangkhut. First, we present evidence supporting the validity of sampling and interpolation schemes described in Section 2. Second, the evolution of  $\zeta$  and  $\Gamma$ , and their effect on  $T$  and  $S$  in our observations is explained using numerical solutions of Equations 9–11. Altogether, these analyses exemplify and expand on the dynamics described in Section 3 and help visualize the mechanisms of NIW generation under fast-moving storms. The role of turbulent mixing in changing  $h$  is discussed briefly.

Mechanisms of NIW generation in model output and observations are compared (Figure 6c) using a time series of the modeled  $(\zeta, \Gamma)/f$  averaged between 14 and 14.5°N (solid lines) and float estimates  $\zeta_{surf}^*/f$  along  $y = 0$  (dashed lines). Much like the idealized solutions in Figures 4 and 5b, the ML response to Mangkhut can be described as a combination of initial forcing by  $\nabla \times \tau$  and later coupling between  $\zeta/f$  and  $\Gamma/f$  by inertial rotation of  $\bar{u}$ . Atmospheric forcing is evidenced by a peak in  $\zeta/f$  under the TC eye, while inertial rotation later transformed this response into a peak in  $\Gamma/f$  (Figure 6c). As  $\bar{u}$  continued to rotate, ML flows reorganized to form minima in  $\zeta/f$  and  $\Gamma/f$  along the TC track (Figures 6a and 6b). At the end of the first inertial cycle, the ML came to have  $\zeta/f \approx 0.25$  and  $\Gamma/f \approx 0$  in both the 3D model and observations (Figure 6c).

Broadly speaking, spatial patterns in  $\|\bar{u}\|$  and  $(\zeta, \Gamma)/f$  in observations (Figure 7) are consistent with those in the 3D model (Figures 6a and 6b). Yet, some notable differences between the modeled and observed ML response exist. For example,  $\Gamma_{surf}^*/f \sim 0.25$  near the leading edge of the TC eye (Figure 7c), but the 3D model yields  $\Gamma_{hycom}/f \sim -0.1$  there (Figure 6b). Available data is insufficient to reliably attribute such differences to potential biases induced by windage and wave motion, our sampling and interpolation scheme, or to processes misrepresented in the 3D model. Nevertheless, patterns in  $\mathbf{u}_{surf}^*$  and  $\mathbf{u}_{mean}^*$  (Figures 7a and 7b) are qualitatively similar to each other, suggesting that windage and wave motion only had a limited impact on  $\mathbf{u}_{surf}^*$ .

With the validity of our observational technique supported by model results, we now put our focus on the coupling between  $\zeta/f$  and  $\Gamma/f$  and how it leads to NIW generation. To test whether observations are consistent with linear theory, Figure 8 compares mapped float data along  $y = 0$  to numerical solutions of Equations 9–11 under idealized forcing and with  $r = 0.5f$ .

Atmospheric forcing by  $\nabla \times \tau$  in Figure 8 corresponds to the reversal of tangential wind between opposite sides of the TC eyewall. The magnitude of  $\nabla \times \tau$  used here agrees with the mean wind stress curl across the TC eye ( $\frac{\langle \tau_{max} \rangle}{MWR} = 2.24 \times 10^{-4} \text{ N m}^{-3}$ , dashed line), where  $MWR = 40 \text{ km}$  is the radius of maximum wind and

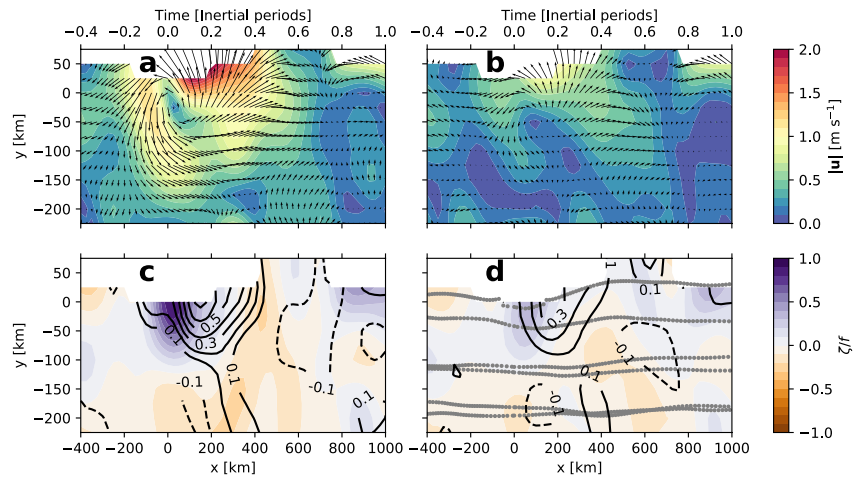


**Figure 7.** Observed mixed layer (ML) dynamics under Mangkhut. (a)  $\mathbf{u}_{surf}^*$  and (b)  $\mathbf{u}_{mean}^*$  show current speeds in color shading. (c)  $\zeta_{surf}^*/f$  and  $\Gamma_{surf}^*/f$ , and (d)  $\zeta_{mean}^*/f$  and  $\Gamma_{mean}^*/f$  show the gradient-based description of ML motions. Black solid contours in (c and d) are for upwelling-favorable values  $\Gamma/f > 0$ , while dashed contours show  $\Gamma/f < 0$ , and gray dots in (d) show the locations of float profiles.

$|\tau_{max}| = C_D \rho_{air} |U_{10}|^2$  was calculated using  $U_{10} = 70 \text{ m s}^{-1}$  (Figure 1),  $\rho_{air} = 1.22 \text{ kg m}^{-3}$ , and  $C_D = 1.5 \times 10^{-3}$  (Zweers et al., 2010).

The magnitude of convergent stresses  $\nabla \cdot \tau < 0$  is set to be artificially low in these simulations (Figure 8a). Although  $\|\nabla \cdot \tau\| \sim \|\nabla \times \tau\|$  in the 3D atmospheric model, the response in  $\Gamma$  that is generated by  $\|\nabla \cdot \tau\|$  is rapidly suppressed by 3D and nonlinear effects and thus does not contribute significantly to NIW generation in the TC wake (Price, 1983; Shay et al., 1989). Lastly, it should be noted that forcing in Figure 8a ignores the gradual weakening of  $\tau$  far from the eyewall, where  $\nabla \times \tau < 0$  and  $\nabla \cdot \tau > 0$ .

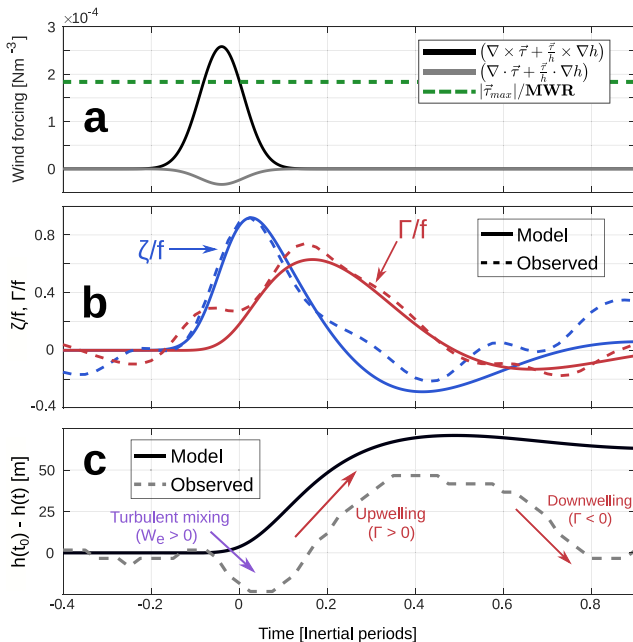


**Figure 8.** Mixed layer response to idealized tropical cyclone (TC)-like atmospheric forcing. (a) Idealized wind forcing (solid lines) used to drive the ML linear model in Equations 9–11 setting  $W_e = \nabla h = 0$  and  $r = 0.5f$ . The dashed green line indicates the mean wind stress curl  $\|\tau_{max}\|/MWR$  of the TC eye. (b) Numerical solutions of  $\zeta/f$  (blue) and  $\Gamma/f$  (red) are compared to observations  $\zeta_{surf}/f$  and  $\Gamma_{surf}/f$  along  $y = 0 \text{ km}$  (Figure 7c). (c) Linear solutions of  $h(t)$  (solid line) are compared to observed displacements of the 27°C isotherm (dashed line).

Agreement between linear solutions and observations in Figure 8 confirms that clockwise rotation of  $\bar{\mathbf{u}}$  (Figure 2b) transformed the wind-forced  $\zeta$  into  $\Gamma$  near the end of the forced stage. Momentum in  $\Gamma$  was later transferred to an inertial anticyclone  $\zeta < 0$  and the cycle continued as shown schematically in Figure 4. Note that the quality of the fit in Figure 8b is sensitive to various model parameters ( $r$ ,  $\nabla \times \tau$ ,  $\nabla \cdot \tau$ ), and initial conditions for ( $\zeta$ ,  $\Gamma$ ,  $h$ ). Nonetheless, this analysis confirms that  $\zeta$  and  $\Gamma$  oscillate in quadrature in observations, the 3D model, and linear theory (Figures 6c and 8b). This robust result comes from the linear terms by which  $f$  couples  $u$  and  $v$  in Equations 6 and 7, and  $\zeta$  and  $\Gamma$  in Equations 9 and 10.

When Earth's rotation transferred  $\zeta$  into  $\Gamma$ , the ML base moved upwards and a NIW was generated (Figures 8c and 9a). Observations show that the 27°C isotherm deepened by  $\sim 25 \text{ m}$  under the TC eye before it shoaled by 75 m as predicted by linear theory (Figure 8c). Initial deepening may be partially explained by turbulent mixing, evidenced by Thorpe scale estimates  $\kappa \sim 10^{-1} \text{ m}^2 \text{ s}^{-1}$  near  $x = 0 \text{ km}$  (Figure 9b). Agreement between the modeled  $\frac{\partial h}{\partial t}$  and observed displacements of the 27°C isotherm behind the TC are consistent with  $\Gamma_{surf}^*$  there (Figure 8c). This result implies that upwelling in the wake of Mangkhut resulted from the near-inertial coupling of  $\zeta$  and  $\Gamma$ , marking the generation of a large amplitude NIW. Moreover, the modeled  $\Gamma$  agrees well with  $\Gamma_{surf}^*$  for all  $t > 0$  (Figure 8b). However,  $\Gamma_{surf}^*$  failed to capture downwelling necessary to displace  $h$  after  $t \approx 0.6$  inertial periods (Figure 8c).

Profiles of  $w^*$  and  $u^*$  in Figure 9a reveal the structure of upwelling in the wake of Mangkhut. There,  $w^*$  reaches  $8 \text{ m hr}^{-1}$  and explains isothermal displacements as large as 75 m around  $x = 350 \text{ km}$ .  $T^*$  shows that isotherms

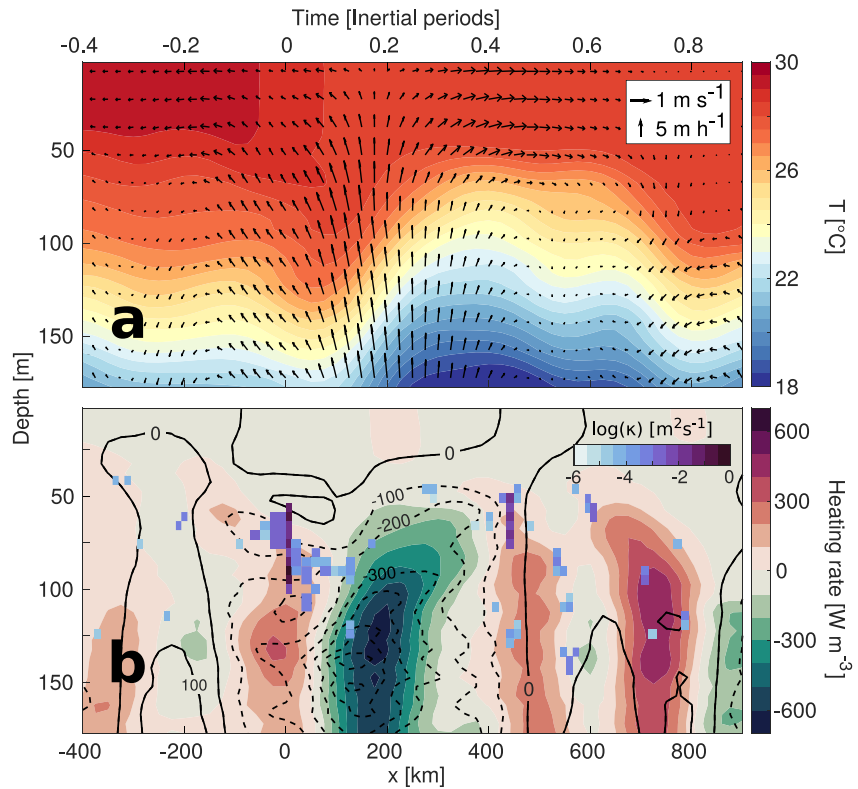


**Figure 9.** (a) Vertical sections of  $T^*$  and  $(u^*, w^*)$  along  $y = 0$  show the generation of a near-inertial wave behind Mangkhut. The vertical component  $w^*$  is magnified for clarity. (b) The Eulerian heating rate  $\frac{\partial H_c}{\partial t}$  estimated using  $\frac{\partial T_{\text{frozen}}^*}{\partial t}$  (color shading) and  $\frac{\partial T_{\text{adv}}^*}{\partial t}$  (black contours), while estimates of  $\kappa$  indicate the intensity of vertical mixing inferred from Thorpe scales in M3 data (note the log scale).

had been lifted by  $\sim 20$  m after  $\sim 0.85$  inertial periods ( $x = 850$  km, Figure 9a), indicating that the oscillatory NIW displacement is  $\sim 55$  m from crest to trough. Net upwelling of isotherms in TC wakes is evidence of geostrophic adjustment (Geisler, 1970; Nilsson, 1995), which is regulated in Equations 10 and 11 by the magnitude of  $r$  for a given atmospheric forcing (Figure 5c).

To test the impacts of advection in setting the ocean stratification behind Mangkhut, as well as the accuracy of inferred 3D flows (Equations 1–3), the Eulerian heating rate  $\frac{\partial H_c}{\partial t} = \rho_0 C_p \frac{\partial T^*}{\partial t}$  is calculated along  $y = 0$  through two different methods (Figure 9b). First, we used a frozen field assumption so that  $\frac{\partial T_{\text{frozen}}^*}{\partial t} = U_{\text{storm}} \frac{\partial T^*}{\partial x}$  (color shading). Second, we used  $\mathbf{u}^*$  and  $w^*$  to calculate the advective contribution  $\frac{\partial T_{\text{adv}}^*}{\partial t} = -u^* \frac{\partial T^*}{\partial x} - v^* \frac{\partial T^*}{\partial y} - w^* \frac{\partial T^*}{\partial z}$  (black contours). Note that the latter expression ignores heating by turbulent mixing, while the frozen field estimate accounts for all observed heat transfer.

Areas of agreement between both estimates of  $\frac{\partial H_c}{\partial t}$  (color shading and black contours in Figure 9b) suggest that heat transfer was locally dominated by the vertical advection term  $w^* \frac{\partial T^*}{\partial z}$  and that the approximation  $w^*$  is adequate. Similarities are particularly good near  $x = 180$  km, where upwelling caused  $\frac{\partial H_c}{\partial t} \sim -500 \text{ W m}^{-3}$ .

Advective estimates of  $\frac{\partial H_c}{\partial t}$  mistakenly predict cooling below 75 m depth around  $x = 0$ , where  $T^*$  shows heating rates as high as  $300 \text{ W m}^{-3}$  (color shading). Disagreement between observed heating and advective estimates below the TC eye may be explained by a possible bias in  $\Gamma_{\text{surf}}^*$  (Figure 6c) but also by vigorous mixing. Thorpe scale estimates  $\kappa \sim 10^{-1} \text{ m}^2 \text{ s}^{-1}$  near  $x = 0$  (Figure 9b) reveal areas where the corresponding turbulent heat flux  $J_q \sim 4,000 \text{ W m}^{-2}$  (Equation 5) could invalidate the assumption that  $\frac{\partial H_c}{\partial t}$  was dominated by advection.

While variations in the ML flow are dominated by near-inertial oscillations (Figure 8),  $\frac{\partial H_c}{\partial t}$  also shows the signature of higher-frequency motions (Figure 9b). Horizontal sections of  $\zeta^*/f$ ,  $\Gamma^*/f$ , and  $N^*$  at 160 m depth (Figure 10) feature nearly parallel, periodic stripes that move away from the storm track toward  $y < 0$ . Dashed black lines

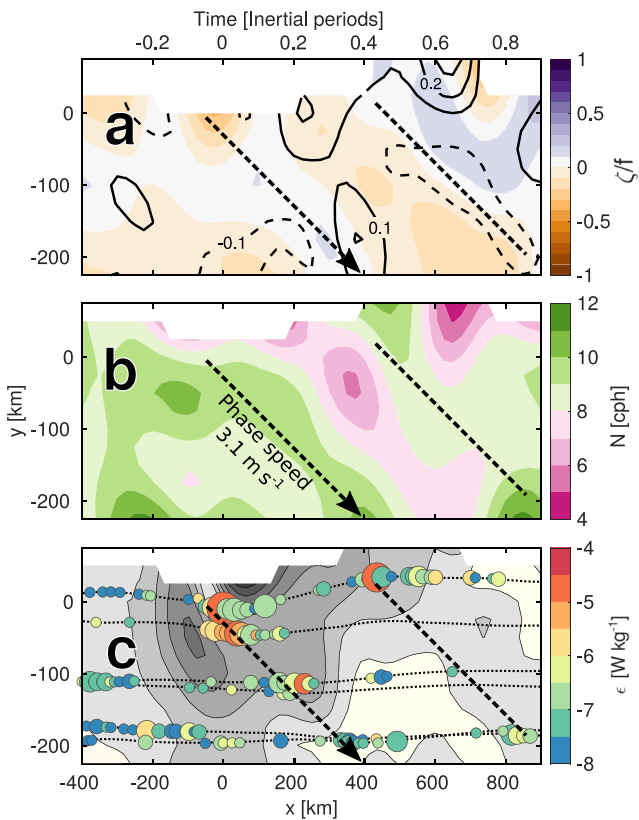


**Figure 10.** Horizontal sections of dynamical variables at 160 m depth. (a)  $\xi^*$  (color) and  $\Gamma^*$  (black contours, negative dashed), (b)  $N^*$ , and (c)  $\|\mathbf{u}_{surf}^* - \mathbf{u}_{mean}^*\|$  (gray shading at 0.2 m s<sup>-1</sup> intervals), which is a proxy for vertical shear at the ML base. The colors of circles in this figure. (c) indicate  $\epsilon$  estimated for individual overturns. The size of circles indicates overturn size (given by the maximum  $d'$ ), which ranges between 5 and 25 m. Thin, dotted lines denote individual float tracks. Note that scales differ in  $x$  and  $y$ .

in Figure 10 help identify this apparent propagation corresponding to a cross-track phase speed  $\sim 3.1$  m s<sup>-1</sup>. While  $\xi^*/f$  and  $\Gamma^*/f$  are linked by the rotation of current vectors (Figure 4),  $\Gamma^*$  and  $N^*$  are linked by isopycnal displacement and straining. Therefore, these three variables offer complementary views of internal wave phase propagation.

The difference between surface and vertically averaged velocities  $\|\mathbf{u}_{surf}^* - \mathbf{u}_{mean}^*\|$  is a proxy for vertical shear below the ML (Figure 10c), which drives turbulent mixing in TC wakes (Price, 1981). Thorpe scale estimates of  $\epsilon$  in individual overturns are shown with colored circles (Figure 10c), with their greatest values and concentration appearing within 100 km of the TC eye. Ahead of the TC, overturns with  $\epsilon < 10^{-7}$  W kg<sup>-1</sup> were sampled at nearly equidistant locations by floats M3, M6, and M0. Conversely, overturns in the TC wake appeared more sporadically and clustered around a few locations, but with most values of  $\epsilon$  ranging between  $3 \times 10^{-7}$  and  $10^{-6}$  W kg<sup>-1</sup>.

## 5. Upper Ocean Thermodynamics Beneath Mangkhut

### 5.1. Mixed Layer Deepening and Turbulent Entrainment

Space-time variations in subsurface  $T$  and  $S$  result from 3D advection, mixing, and interactions with the atmosphere. In the case of intense, fast-moving TCs like Mangkhut ( $U_{storm}/c_g \sim 2$ ), shear-driven mixing at the ML base is expected to dominate upper ocean cooling (D'Asaro, 2003; Vincent et al., 2012). This process is evidenced by float measurements of  $T$  averaged between 0.5 and 1.5 m depth (Figure 11a), which show a general cooling trend during TC passage.

In particular, 1-m binned profiles of  $T$ ,  $S$  and potential density ( $\sigma_\theta$ ) from float M3 show a clear, gradual deepening of the ML base between  $x = -250$  and  $x = 0$  km (Figures 11b–11d). Successive float profiles in Figures 11b–11d show cooling trends in SST but increasing sea surface salinity (SSS) and  $\sigma_\theta$  as the ML deepened. This corresponds to entrainment of cold, salty water from below and implies that a fraction of turbulent kinetic energy in wind-driven currents was used to raise the potential energy (PE) of the water column. In fact, density data ( $\rho$ ) from floats M1 and M3 indicate that  $PE_{-60}^0 = \int_{-60}^0 \rho g z dz$  in the upper 60 m increased by  $\sim 9$  and  $10 \times 10^3$  J m<sup>-2</sup> between  $x = -200$  and 200 km, respectively.

As further evidence of the vigorous turbulence that transformed ocean thermodynamics beneath Mangkhut, vertical profiles of  $\sigma_\theta$  feature  $\sim 10$  m-tall regions with unstable stratification (i.e.,  $\frac{\partial \sigma_\theta}{\partial z} > 0$ , Figure 11d). Thorpe scale estimates (see Section 2.2) in Figures 9b and 10c indicate the contribution of these density overturns to ocean turbulence. Overall, the distribution and magnitude of turbulent patches agree with the timing of ML deepening and SST cooling (Figures 8c and 11a). We estimate the turbulent heat flux  $J_q \sim 4000$  W m<sup>-2</sup> out of the ML for float M3 near  $x = 0$  km (given  $\kappa \sim 0.1$  m<sup>2</sup> s<sup>-1</sup> and  $\frac{\partial T}{\partial z} \sim 0.01^\circ\text{C m}^{-1}$  in Equation 5). For a ML with  $h = 40$  m, this value of  $J_q$  corresponds to an SST cooling rate  $\sim -0.1^\circ\text{C hr}^{-1}$ , consistent with observations in Figure 11a. The corresponding salinity flux  $\kappa \frac{\partial S}{\partial z}$  is  $\sim 1 \times 10^{-3}$  psu m s<sup>-1</sup> out of the ML, equivalent to a rate of increase  $\sim 0.1$  psu hr<sup>-1</sup>, also consistent with observations by M3 (Figure 12a).

After storm passage, SSS (SST) had increased (decreased) for all floats (Figures 11a and 12a), indicating widespread mixing of the upper ocean beneath Mangkhut. In fact, plan views of near-surface  $T^*(x, y)$  and  $S^*(x, y)$  in Figure 13 reveal a narrow and asymmetric wake of cold, salty water. This indicates that SST cooling was dominated by turbulent mixing and is consistent with greater windwork and current speeds for  $y > 0$  (Figures 6a and 7a and 7b, Chang & Anthes, 1978; Price, 1981). Furthermore, gradients  $\frac{\partial T^*}{\partial x}$  and  $\frac{\partial S^*}{\partial t}$  (not shown) indicate that maximum mixing rates occurred within 100 km of the TC eye, in agreement with Thorpe scale estimates in Figures 9b and 10c.

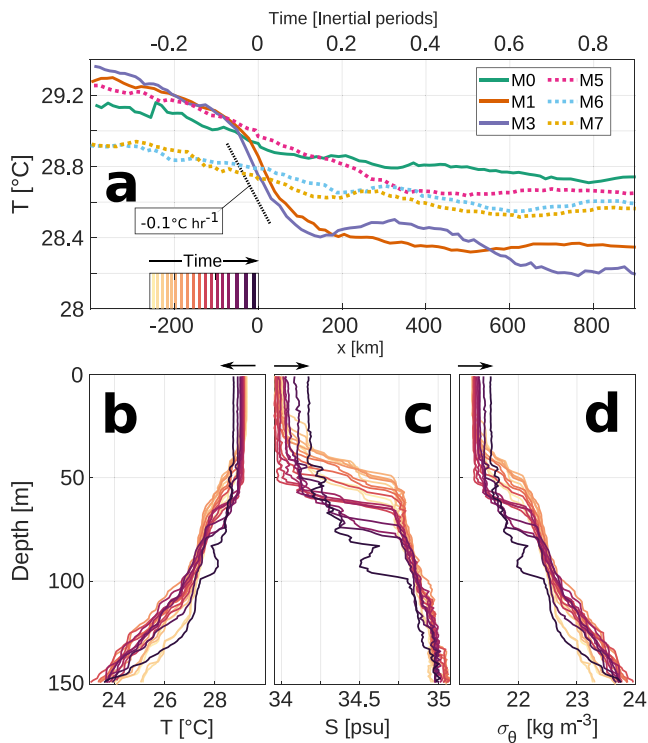


**Figure 11.** Sea surface temperature (SST) cooling by turbulent entrainment. (a) SST measured by all floats as a function of along-track distance  $x$ . 1-m binned profiles of (b)  $T$ , (c)  $S$ , and (d) potential density  $\sigma_\theta$  measured by float M3 between  $x = -250$  and  $x = 0$ . Individual profiles shown in the lower panels are color coded by their position in  $x$  (color bar in panel a).

The impact of precipitation on  $S$  in the upper 5 m is opposite to that of mixing and thus can be assessed from Figure 12a, as floats M5, M6 and M7 sampled sharp decreases in near-surface  $S$  between  $x = -250$  and  $x = -150$  km. To examine the impacts of rainfall in near-surface  $T$  and  $S$ , we interpolated data from the Integrated Multi-Satellite Retrievals for Global Precipitation Measurement (IMERG, Huffman et al., 2015) onto the times and locations of float measurements. Estimated hourly rates of precipitation and cumulative rainfall integrated since floats were at  $x = -400$  km show that all floats experienced considerable precipitation (Figure 12b).

Despite receiving more freshwater ( $\sim 300$  mm) than any other floats, time series of near-surface  $S$  from M1 and M3 do not feature noticeable decreases attributable to precipitation (Figure 12). For precipitation to noticeably impact measurements of  $S$ , surface rain layers must form and remain stable for a period of time long enough ( $>30$  min) to be sampled by floats. However, this is only possible when buoyancy production by rainfall is greater than buoyancy mixing rates that diffuse salinity gradients (E. J. Thompson et al., 2019). Given that floats M1 and M3 were near the TC track and experienced the greatest turbulence rates (Figure 10c), it is likely that sudden SSS freshening by rainfall was quickly mixed before it could be sampled.

Successive profiles of  $T$  and  $S$  by float M7 (Figure 14) detail the process of rain layer formation and their subsequent destruction by turbulent mixing. Each row of plots in this sequence shows 5 consecutive profiles spanning  $\sim 3$  hr ( $\sim 75$  km). At the beginning, float profiles ranging from  $x = -246$  to  $x = -168$  km show a well-mixed upper ocean with no vertical gradients in  $T$  or  $S$  (Figures 14a and 14b). Later on, a layer of water with low  $T$  and  $S$  formed in the upper 5 m around  $x = -140$  km (black line) but was gradually mixed and deepened over the following casts (Figures 14c and 14d). This rain layer

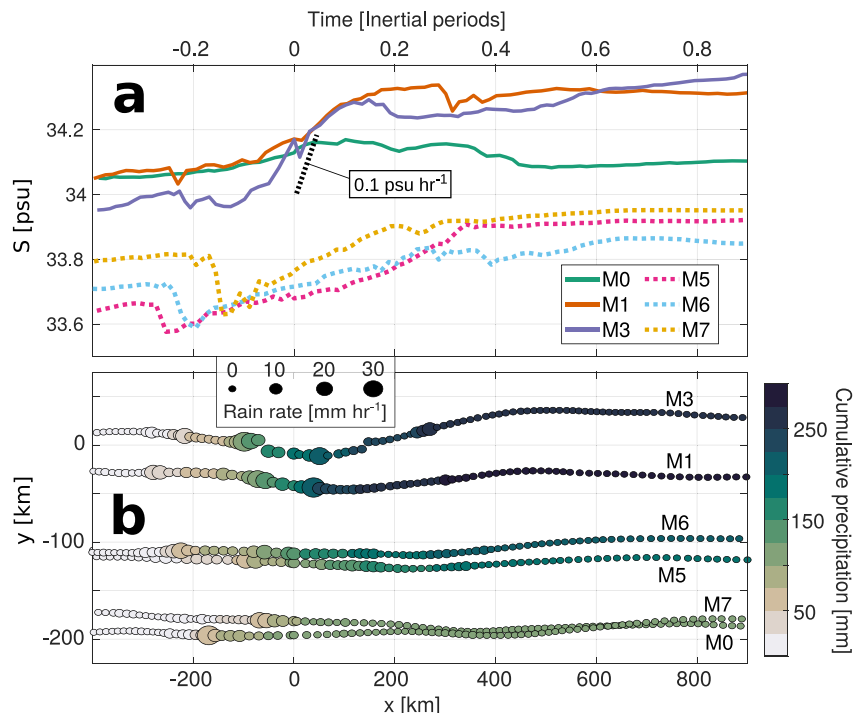


**Figure 12.** (a)  $S$  averaged in the upper 5 m along float tracks increases as a response to mixing of subsurface waters and decreases due to rainfall. (b) IMERG data show rain rates and cumulative precipitation along float trajectories.

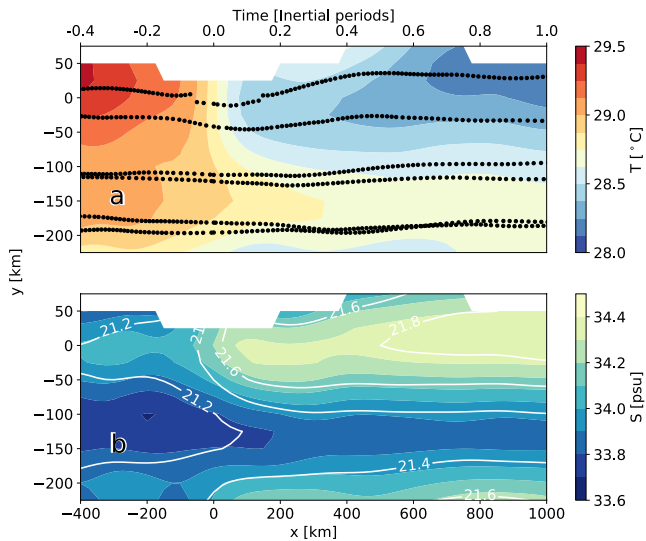


**Figure 13.** Plan view of (a)  $T^*$  and (b)  $S^*$  averaged over the upper 5 m. Black dots show the locations of each profile, while white contours in (b) show values of  $\sigma_\theta$  in units of  $\text{kg m}^{-3}$ .

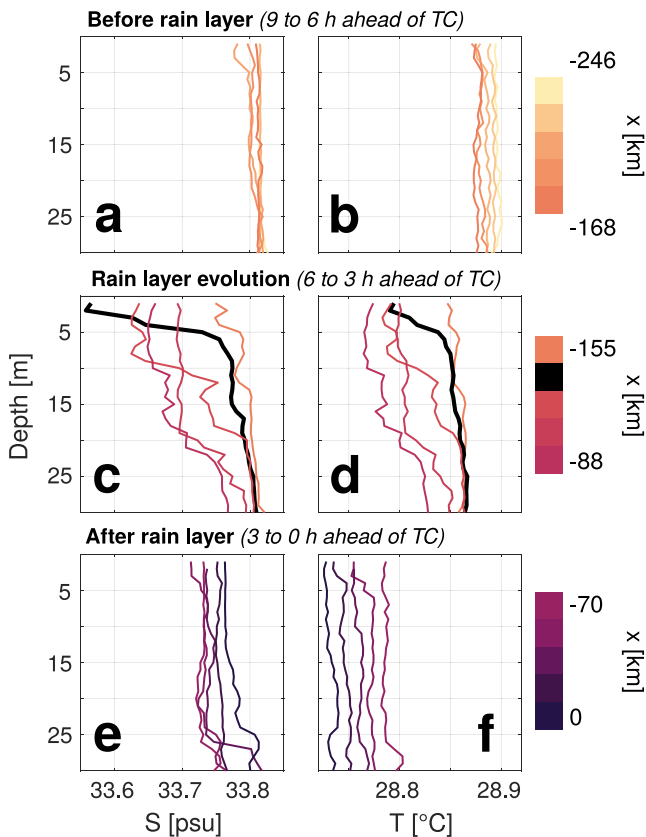


**Figure 14.** Three stages of rain layer evolution. Each row shows five consecutive profiles of  $T$  and  $S$  (color-coded by along-track position  $x$ ) measured by float M7 over a  $\sim 3$  hr period. (a)  $S$  and (b)  $T$  before rainfall effects were noticeable. (c and d) show the formation of a rain layer (black line) and its gradual diffusion to greater depths. On (e) and (f), turbulent mixing has mostly de-stratified the upper ocean.

accounts for the sharp decrease in SSS measured by M7 (Figure 12a), while the subsequent increase in SSS was consistent with mixing of cold, salty water from below. Roughly four hours (near  $x = -50$  km) after its formation, there was little to no indication left that a rain layer had formed around float M7 (Figures 14e and 14f).

Under fast-moving and high-intensity TCs like Mangkhut, precipitation can counteract some impacts of mixing, increasing  $S$  and decreasing  $\sigma_\theta$  in the ML (Huang et al., 2009; Reul et al., 2021). Mixing a rain layer with  $S = 0$  and thickness  $\Delta h_{rain} = 0.3$  m (Figure 12b) into a ML with  $S = 34$  psu and  $h = 40$  m would decrease SSS by 0.2 psu and surface  $\sigma_\theta$  by  $0.15 \text{ kg m}^{-3}$ . This is equivalent to  $\sim 60\%$  of the observed increase in SSS near the TC track (Figure 12a) and  $\sim 25\%$  of the observed change in surface  $\sigma_\theta$  (Figure 13b). In the case of Mangkhut, the SSS and surface  $\sigma_\theta$  anomalies induced by rainfall were  $\sim -30\%$  and  $\sim -15\%$  as large as those caused by mixing.

As an indirect effect of precipitation on air-sea interaction under TCs, we now consider the energetics associated with rain layer destruction by mixing. To estimate this, we compare  $PE$  of a water column before and after buoyancy anomalies in a rain layer of thickness  $\Delta h_{rain}$  have been mixed down to the ML base. For  $\Delta h_{rain} = 0.3$  m,  $PE$  in the upper 60 m changes by  $\sim 10^3 \text{ J m}^{-2}$ , roughly 10% of the change estimated between  $x = -200$  and  $x = 200$  km for floats M1 and M3. This suggests that rain layer destruction can take up  $\sim 10\%$  of turbulent kinetic energy under TCs, therefore inhibiting further SST cooling from mixing across the ML base (Jourdain et al., 2013; Smyth et al., 1997).

## 5.2. Turbulent Mixing Effects on Stratification

While the impacts of TC-driven turbulence are most noticeable in the formation of cold and salty wakes (Figure 13), thermocline mixing by TCs helps regulate ocean heat uptake and transport (Jansen et al., 2010; Mei et al., 2013; Srivier & Huber, 2007). To assess these effects, modellers often make assumptions about the spatial and temporal extent of anomalous  $\kappa$  driven by TCs. Below, we analyze observed changes in the  $T$ - $S$  relations to infer  $\kappa$  in the TC wake. In this way, we retrieve information about TC-driven mixing that may not be inferred from surface or ML thermodynamics alone.

Changes in  $T$ - $S$  relations for floats M1 and M3 (Figure 15a) resulted from a combination of turbulence, 3D advection, and atmospheric fluxes. However, the effects of turbulence are distinguishable from others because mixing between two water masses produces a weighted average of the original  $T$ - $S$  properties across contiguous layers (Alford et al., 1999; Hautala et al., 1996; Moum et al., 2003). For example, we consider the changes in average  $T$ - $S$  properties measured by float M3 within the ranges  $200 = x \leq 400$  km and  $400 = x \leq 600$  km (dashed and solid lines respectively in Figure 15b). To assess the role of turbulence in setting the evolution between the two  $T$ - $S$  profiles in Figure 15b, we compare observations to the evolution predicted by

$$\frac{\partial T}{\partial t} \sim \kappa \frac{\partial^2 T}{\partial z^2} \quad (14)$$

$$\frac{\partial S}{\partial t} \sim \kappa \frac{\partial^2 S}{\partial z^2}. \quad (15)$$

Equations 14 and 15 ignore the effects of 3D advection and air-sea interaction, and thus describe only the effects of mixing on  $T$ - $S$  relations. Taking

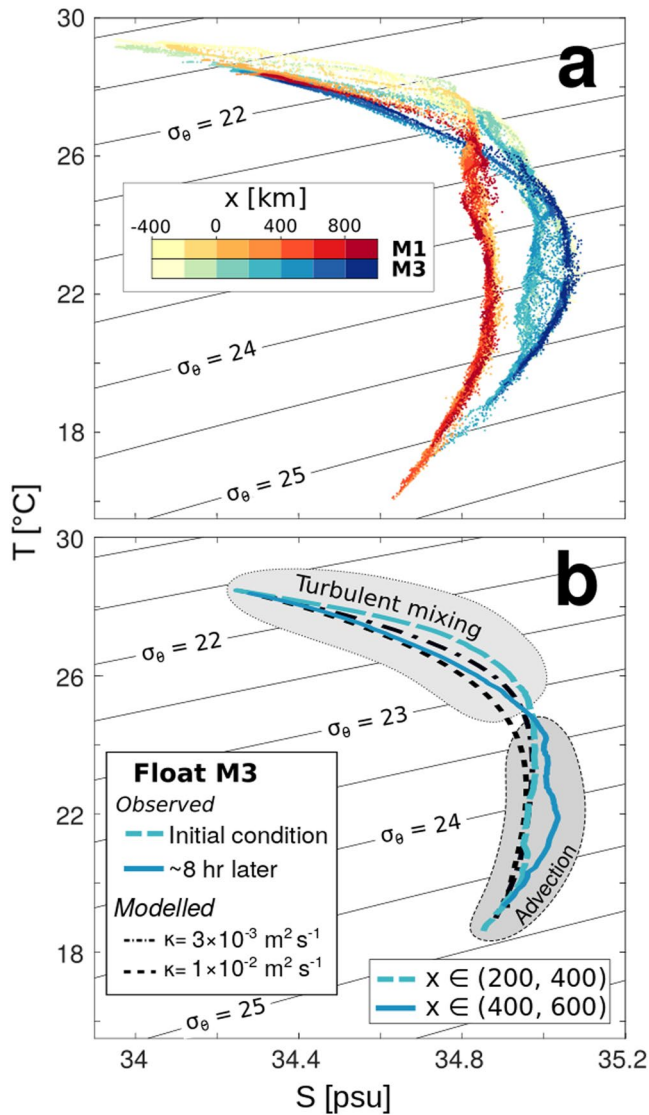


**Figure 15.** (a)  $T$ - $S$  profiles measured by floats M1 and M3 are color-coded by  $x$ . (b) Mean  $T$ - $S$  profiles for  $x \in (200, 400)$  km (dashed line) and  $x \in (400, 600)$  km (solid line) by float M3 show transformations caused throughout an 8 hr period. Black dashed lines show  $T$ - $S$  properties modeled using Equations 14 and 15 under the initial condition  $x \in (200, 400)$  km and different values of  $\kappa$ .

the profile observed by M3 for  $x \in (200, 400)$  km as our initial condition and setting  $\kappa = 3 \times 10^{-3}$  and  $1 \times 10^{-2} \text{ m}^2 \text{ s}^{-1}$  over 8 hr (0.2 inertial periods) yields the  $T$ - $S$  profiles shown in black dashed lines (Figure 15b). Numerical solutions to Equations 14 and 15 used boundary conditions  $\frac{\partial}{\partial z} = 0$  at  $z = 0$  and  $z = 180$  m, implying no flux through the boundaries. Results agree well with the observed  $T$ - $S$  changes for  $\sigma_\theta < 23.2 \text{ kg m}^{-3}$  but fail to explain observations at greater densities (Figure 15b). More precisely, note that for  $\sigma_\theta > 23.5 \text{ kg m}^{-3}$ , the observed  $S$  was beyond the range of  $S$  in the initial condition. Such a transformation requires input of high- $S$  water from elsewhere and hence cannot result from vertical mixing. Altogether, these analyses suggest mixing dominated watermass transformations down to  $\sim 110$  m depth between  $x = 200$  and  $x = 600$  km, while 3D advection had greater impacts below.

Values  $\kappa > 10^{-3} \text{ m}^2 \text{ s}^{-1}$  inferred from this analysis are 3–10 times greater than the majority of Thorpe scale estimates between  $x = 200$  and  $600$  km, whose mean value is  $7.1 \times 10^{-4} \text{ m}^2 \text{ s}^{-1}$  (Figure 9b). This is not a large discrepancy given the uncertainty of Thorpe scale estimates and the small number ( $< 30$ ) of overturns detected in this range of  $x$ . Vertical profiles of  $T(z)$  (not shown) that make up modeled  $T$ - $S$  relationships in Figure 15b feature negligible cooling at the surface level, but cooling of  $\sim 0.2^\circ\text{C}$  that peaks near 40 m depth. Areas of mixing-induced warming as large as  $\sim 0.1^\circ\text{C}$  appear between 60 and 100 m depth, but the majority of heat transferred downwards in solutions of Equation 14 accumulated below 150 m, where our observations cannot help derive estimates of  $\kappa$  (Figure 15b). Further observations are needed to better characterize the vertical extent of mixing-induced warming during this stage shortly after TC passage.

To assess the long-term impacts of 'residual' mixing in the TC wake (Figure 15b), we use  $\kappa = 3 - 10 \times 10^{-3} \text{ m}^2 \text{ s}^{-1}$  to compute  $J_q$  across the  $26^\circ\text{C}$  isotherm (approximately 60 m depth), yielding mean values  $\langle J_q \rangle \approx 1,900 \pm 1000 \text{ W m}^{-2}$  within  $200 < x < 600$  km and  $-50 < y < 50$  km. This value of is roughly three times as large as the downwelling shortwave radiative flux under clear skies in this area, which peaked near  $700 \text{ W m}^{-2}$  in shipboard observations made when the floats were deployed. Given that SST cooling typically stops only a few hours after TC passage (Figure 11a), it is often assumed that TC-driven mixing stops then too. Nevertheless, these measurements (Figure 15b) indicate that the vertical redistribution of heat by TC-driven turbulence lasts beyond what SST data alone would suggest. The persistence and vertical distribution of heat content anomalies days to weeks after Mangkhut was studied by Johnston et al. (2020), who highlighted advection of subsurface anomalies by the North Equatorial Current and potential interactions with subsequent TCs.

## 6. Discussion

The 3D ocean response to Super Typhoon Mangkhut was reconstructed and diagnosed using data from profiling floats. We find general agreement between interpolated fields and a 3D model (Figures 6 and 7). A linear model using  $\zeta$  and  $\Gamma$  instead of  $\bar{u}$  to describe ML dynamics helped interpret measurements and identify the mechanisms driving NIW generation (Figures 8 and 9). Lastly, estimates of  $\kappa$  and  $\varepsilon$  based on  $T$  and  $S$  data provides insight about the spatiotemporal persistence of TC-driven mixing and impacts to upper ocean thermodynamics (Figures 9b, 10c, 14, and 15b).

### 6.1. Linear ML Dynamics and Inertial Pumping

Our analyses describe the mechanism responsible for NIW generation by TCs. For the first time, the dynamics of inertial pumping were reduced to a set of ordinary differential Equations 9–11 for  $\zeta$  and  $\Gamma$ , while observations of  $\zeta$  and  $\Gamma$  were found to be in agreement with both linear theory and a 3D model (Figures 6 and 8). The theoretical and observational results of this study are in close alignment with early analyses by Geisler (1970) and Price (1981, 1983), meaning that we have not unveiled any new physics. Rather, the significance of this study is in pointing out the inertial coupling between  $\zeta$  and  $\Gamma$  as the essence of inertial pumping and in using observations to show those physics at work under a TC of extreme intensity (Figure 2c).

Past studies have inferred the 3D structure of upper ocean features powered by TCs (Jacob et al., 2000; Price et al., 1994; Sanabia & Jayne, 2020). Here, the ( $\zeta$ ,  $\Gamma$ ) framework presented in Section 3 helped us to unambiguously relate observed isothermal displacements to TC forcing (Figures 8 and 9). Equations 9–11 can relate storm morphology (represented by  $\nabla \times \tau$  and  $\nabla \cdot \tau$ ) to patterns in NIW generation in a 1D framework. While our results validate Equations 9–11 in reproducing upwelling and NIW generation by fast-moving TCs, future studies may test it for slow-moving TCs and storms with different morphologies. General nonlinear dynamical models based on  $\zeta$  and  $\Gamma$  (see e.g., Névir & Sommer, 2009) may facilitate such studies by clarifying the roles of pressure gradients and nonlinear terms.

### 6.2. Float-Based Estimates of $\zeta$ and $\Gamma$

Float estimates of  $\zeta$  and  $\Gamma$  for  $x > 500$  km in TC-following coordinates do not capture  $\Gamma < 0$  necessary for downwelling evidenced by  $T^*$  (Figures 8c and 9). This is likely due to the loss of coherence by NIWs in the TC wake, since derivatives  $\frac{\partial u^*}{\partial y}$  and  $\frac{\partial v^*}{\partial y}$  are set by differences in measurements made more than 200 km and 12 hr apart (Figures 1 and 2). Such biases in  $(\zeta_{surf}^*, \Gamma_{surf}^*)/f$  affect the value  $r = 0.5f$  used for numerical solutions in Figure 8, which is considerably higher than values  $\sim 0.2f$  commonly used to reproduce  $\bar{u}$  under extratropical storms (Alford, 2001; D'Asaro, 1985; Pollard & Millard, 1970). Past studies have argued that  $r$  is likely greater in TC wakes due to increased NIW energy flux divergence caused by the point-like nature of TC forcing (Kundu & Thomson, 1985) and interactions with background motions (Guan et al., 2014). However, aforementioned uncertainties in our estimates ( $\zeta_{surf}^*, \Gamma_{surf}^*$ ) complicate interpretations of the significance of the value  $r = 0.5f$  used here and its relation to NIW dynamics. A detailed analysis of NIW properties using this data set over longer timescales and without the assumptions implied by our coordinate transformation can be found in Johnston et al. (2021).

### 6.3. Float-Based Descriptions of Mixing

Vertical profiles of  $T$  and  $S$  (Figures 11 and 14) detail mixing processes that modulate storm development. Thorpe scale estimates of  $\kappa$  and  $\varepsilon$  (Figures 9 and 10) provide the spatial distribution of mixing and potential impacts to air-sea interactions. While turbulent heat fluxes have been calculated directly using Lagrangian instruments (D'Asaro, 2003), the indirect approach followed here allows near real-time monitoring with potential applications in forecasting. Moreover, the watermass transformation analysis in Figure 15 and inferred turbulent mean heat fluxes  $J_q \approx 1,900 \pm 1,000$  W m<sup>-2</sup> across the 26°C isotherm in the TC wake show that subsurface redistribution of heat by mixing may persist after SST stabilizes. This emphasizes the importance of in-situ turbulence estimates in studies aiming to improve parameterizations used in studies of TC-climate interaction (Gutiérrez Brizuela et al., 2023; Korty et al., 2008; Srivier & Huber, 2007).

Insufficient spatial resolution in numerical models can cause them to underestimate the intensity of TC winds (Walsh et al., 2007), subsequent upwelling, and NIW generation (Vincent et al., 2012). Likewise, it is unclear whether mixing parameterizations used by models can reproduce the full set of impacts reported here and others that may remain undetected. For example, accurate representation of mixing in rain layers (Figure 14) and barrier layers (Balaguru et al., 2012; Rudzin et al., 2019) is challenging but necessary to avoid biases in forecasts of storm intensity (Hlywiak & Nolan, 2019). These and other intricacies associated with TC-driven mixing and NIW generation, including their long-term impacts on ocean thermodynamics, have yet to be comprehensively described in observations. Analyses presented in Sections 4 and 5 show how data from autonomous platforms can provide insight about the multiscale ocean response to TCs. Such profiling float measurements are crucial to accurately constrain the role of TCs in global budgets of mixing and internal wave energy.



## 7. Conclusions

Formulating the linear ML dynamics using  $\zeta$  and  $\Gamma$  in Equations 9–11 yields a direct statement of inertial pumping and explains NIW generation behind TCs. This gradient-based view shows that the clockwise rotation of currents rearranges  $(u, v)$  so that  $\zeta$  evolves into  $\Gamma$ , and  $\Gamma$  into  $-\zeta$  (Figure 4). In these cycles,  $\zeta$  and  $\Gamma$  remain in quadrature as are  $u$  and  $v$  for NIWs. ML currents in observations and a 3D model of Mangkhut followed this pattern, which also controlled  $w$  in the TC wake (Figures 6 and 8).

Our analyses include indirect estimates of ocean mixing and its effects. Progressive changes in profiles of  $T$  and  $S$  indicate that SST cooling beneath Mangkhut was dominated by turbulent entrainment into the ML (Figures 11 and 13). Thorpe scale estimates in regions of unstable stratification show active mixing ahead, under, and behind Mangkhut but was most vigorous near the TC eye (Figure 10c), where we estimate  $\kappa \sim 10^{-1} \text{ m}^2 \text{ s}^{-1}$ . Such values of  $\kappa$  would produce to heat fluxes of  $\sim 4 \times 10^3 \text{ W m}^{-2}$  across the ML base (Figure 9) and can explain the observed SST cooling rate  $\sim 0.1^\circ\text{C hr}^{-1}$  (Figure 11a). Likewise, the corresponding salinity flux  $\kappa \frac{\partial S}{\partial z} \sim 2 \times 10^{-3} \text{ psu m s}^{-1}$  explains an increase of  $\sim 0.1 \text{ psu hr}^{-1}$  in SSS, roughly the same as the greatest rates in our observations (Figure 12a). Furthermore, our measurements highlight the effects of near-surface rain layers (Figure 14), whose diffusion into the ML was estimated to use  $\sim 10\%$  of the potential energy change associated with mixing near the TC track. Lastly, we document the continued transformation of watermass characteristics hundreds of kilometers behind the TC with diffusivities  $\kappa > 10^{-3} \text{ m}^2 \text{ s}^{-1}$  down to  $\sim 110 \text{ m}$  depth (Figure 15).

## Data Availability Statement

Float data are available at the PISTON data site <https://www-air.larc.nasa.gov/cgi-bin/ArcView/camp2ex?TRAJECTORY=1JOHNSTON.SHAUN/> and TC best track data are available from the JTWC at <https://www.metoc.navy.mil/jtwc/jtwc.html?western-pacific> (Mangkhut was storm 26 of 2018). Coupled ocean-atmosphere model results are available at <https://doi.org/10.5281/zenodo.4134671>.

## Acknowledgments

This work is supported by grant NA17OAR4310259 from the Climate Variability and Predictability program at NOAA, and Grants N00014163085 and N000141613073 from the Office of Naval Research's PISTON initiative, which are components of the international Years of the Maritime Continent program. We are grateful to the master, crew, and science party on *R/V Thomas Thompson* for their help in deploying floats. The Instrument Development Group at the Scripps Institution of Oceanography designed, prepared, and monitored the SOLO-II floats. N.G.B. is funded by Consejo Nacional de Ciencia y Tecnología (CONACyT) and UC Mexus. E.J.T. contributes effort with funding from the NOAA Weather Program Office's Precipitation Prediction Grand Challenge. Without implying their endorsement, we thank Kristin Zeiden, Nathalie Zilberman, and William R. Young for their valuable comments.

## References

- Alford, M. H. (2001). Internal swell generation: The spatial distribution of energy flux from the wind to mixed layer near-inertial motions. *Journal of Physical Oceanography*, 31(8), 2359–2368. [https://doi.org/10.1175/1520-0485\(2001\)031<2359:ISGTS2D>2.0.CO;2](https://doi.org/10.1175/1520-0485(2001)031<2359:ISGTS2D>2.0.CO;2)
- Alford, M. H., & Gregg, M. C. (2001). Near-inertial mixing: Modulation of shear, strain and microstructure at low latitude. *Journal of Geophysical Research*, 106(C8), 16947–16968. <https://doi.org/10.1029/2000JC000370>
- Alford, M. H., Gregg, M. C., & Ilyas, M. (1999). Diapycnal mixing in the Banda Sea: Results of the first microstructure measurements in the Indonesian throughflow. *Geophysical Research Letters*, 26(17), 2741–2744. <https://doi.org/10.1029/1999GL002337>
- Alford, M. H., Gregg, M. C., & Merrifield, M. A. (2006). Structure, propagation, and mixing of energetic baroclinic tides in Mamala Bay, Oahu, Hawaii. *Journal of Physical Oceanography*, 36(6), 997–1018. <https://doi.org/10.1175/JPO2877.1>
- Asselin, O., & Young, W. R. (2020). Penetration of wind-generated near-inertial waves into a turbulent ocean. *Journal of Physical Oceanography*, 50(6), 1699–1716. <https://doi.org/10.1175/JPO-D-19-0319.1>
- Balaguru, K., Chang, P., Saravanan, R., Leung, L. R., Xu, Z., Li, M., & Hsieh, J.-S. (2012). Ocean barrier layers' effect on tropical cyclone intensification. *Proceedings of the National Academy of Sciences*, 109(36), 14343–14347. <https://doi.org/10.1073/pnas.1201364109>
- Balmforth, N., Llewellyn Smith, S. G., & Young, W. (1998). Enhanced dispersion of near-inertial waves in an idealized geostrophic flow. *Journal of Marine Research*, 56(1), 1–40. <https://doi.org/10.1357/002224098321836091>
- Chang, S. W., & Anthes, R. A. (1978). Numerical simulations of the ocean's nonlinear, baroclinic response to translating hurricanes. *Journal of Physical Oceanography*, 8(3), 468–480. [https://doi.org/10.1175/1520-0485\(1978\)008<0468:NSOTON>2.0.CO;2](https://doi.org/10.1175/1520-0485(1978)008<0468:NSOTON>2.0.CO;2)
- Chen, S. S., & Curcic, M. (2016). Ocean surface waves in Hurricane Ike (2008) and Superstorm Sandy (2012): Coupled model predictions and observations. *Ocean Modelling*, 103, 161–176. <https://doi.org/10.1016/j.ocemod.2015.08.005>
- D'Asaro, E. A. (1985). The energy flux from the wind to near-inertial motions in the surface mixed layer. *Journal of Physical Oceanography*, 15(8), 1043–1059. [https://doi.org/10.1175/1520-0485\(1985\)015<1043:TEFFTW>2.0.CO;2](https://doi.org/10.1175/1520-0485(1985)015<1043:TEFFTW>2.0.CO;2)
- D'Asaro, E. A. (1989). The decay of wind-forced mixed layer inertial oscillations due to the  $\beta$  effect. *Journal of Geophysical Research*, 94(C2), 2045–2056. <https://doi.org/10.1029/JC094iC02p02045>
- D'Asaro, E. A. (2003). The ocean boundary layer below Hurricane Dennis. *Journal of Physical Oceanography*, 33(3), 561–579. [https://doi.org/10.1175/1520-0485\(2003\)033<0561:TOBLBH>2.0.CO;2](https://doi.org/10.1175/1520-0485(2003)033<0561:TOBLBH>2.0.CO;2)
- D'Asaro, E. A., Eriksen, C. C., Levine, M. D., Paulson, C. A., Niiler, P., & Van Meurs, P. (1995). Upper-ocean inertial currents forced by a strong storm. Part I: Data and comparisons with linear theory. *Journal of Physical Oceanography*, 25(11), 2909–2936. [https://doi.org/10.1175/1520-0485\(1995\)025<2909:UOICFB>2.0.CO;2](https://doi.org/10.1175/1520-0485(1995)025<2909:UOICFB>2.0.CO;2)
- Davis, R. E. (1985). Objective mapping by least squares fitting. *Journal of Geophysical Research*, 90(C3), 4773–4777. <https://doi.org/10.1029/JC090iC03p04773>
- Davis, R. E., Sherman, J., & Dufour, J. (2001). Profiling ALACEs and other advances in autonomous subsurface floats. *Journal of Atmospheric and Oceanic Technology*, 18(6), 982–993. [https://doi.org/10.1175/1520-0426\(2001\)018<0982:PAAOAI>2.0.CO;2](https://doi.org/10.1175/1520-0426(2001)018<0982:PAAOAI>2.0.CO;2)
- Dillon, T. M. (1982). Vertical overturns: A comparison of thorpe and Ozmidov length scales. *Journal of Geophysical Research*, 87(C12), 9601–9613. <https://doi.org/10.1029/JC087iC12p09601>
- Dunckley, J., Koseff, J., Steinbuck, J., Monismith, S., & Genin, A. (2012). Comparison of mixing efficiency and vertical diffusivity models from temperature microstructure. *Journal of Geophysical Research*, 117(C10). <https://doi.org/10.1029/2012JC007967>

- Ekman, V. W. (1905). On the influence of the earth's rotation on ocean-currents.
- Emanuel, K. A. (1999). Thermodynamic control of hurricane intensity. *Nature*, *401*(6754), 665–669. <https://doi.org/10.1038/44326>
- Emanuel, K. A. (2001). Contribution of tropical cyclones to meridional heat transport by the oceans. *Journal of Geophysical Research*, *106*(D14), 14771–14781. <https://doi.org/10.1029/2000JD900641>
- Emanuel, K. A. (2005). Increasing destructiveness of tropical cyclones over the past 30 years. *Nature*, *436*(7051), 686–688. <https://doi.org/10.1038/nature03906>
- Fedorov, A. V., Brierley, C. M., & Emanuel, K. (2010). Tropical cyclones and permanent El Niño in the early Pliocene epoch. *Nature*, *463*(7284), 1066–1070. <https://doi.org/10.1038/nature08831>
- Ferron, B., Mercier, H., Speer, K., Gargett, A., & Polzin, K. (1998). Mixing in the romanche fracture zone. *Journal of Physical Oceanography*, *28*(10), 1929–1945. [https://doi.org/10.1175/1520-0485\(1998\)028<1929:MITRFZ>2.0.CO;2](https://doi.org/10.1175/1520-0485(1998)028<1929:MITRFZ>2.0.CO;2)
- Galbraith, P. S., & Kelley, D. E. (1996). Identifying overturns in ctd profiles. *Journal of Atmospheric and Oceanic Technology*, *13*(3), 688–702. [https://doi.org/10.1175/1520-0426\(1996\)013<0688:IOICP>2.0.CO;2](https://doi.org/10.1175/1520-0426(1996)013<0688:IOICP>2.0.CO;2)
- Gargett, A., & Garner, T. (2008). Determining thorpe scales from ship-lowered CTD density profiles. *Journal of Atmospheric and Oceanic Technology*, *25*(9), 1657–1670. <https://doi.org/10.1175/2008JTECH0541.1>
- Geisler, J. E. (1970). Linear theory of the response of a two layer ocean to a moving hurricane. *Geophysical & Astrophysical Fluid Dynamics*, *1*(1–2), 249–272. <https://doi.org/10.1080/03091927009365774>
- Gill, A. (1984). On the behavior of internal waves in the wakes of storms. *Journal of Physical Oceanography*, *14*(7), 1129–1151. [https://doi.org/10.1175/1520-0485\(1984\)014<1129:OTBOIW>2.0.CO;2](https://doi.org/10.1175/1520-0485(1984)014<1129:OTBOIW>2.0.CO;2)
- Glenn, S., Miles, T., Seroka, G., Xu, Y., Forney, R., Yu, F., et al. (2016). Stratified coastal ocean interactions with tropical cyclones. *Nature Communications*, *7*(1), 1–10. <https://doi.org/10.1038/ncomms10887>
- Guan, S., Zhao, W., Huthnance, J., Tian, J., & Wang, J. (2014). Observed upper ocean response to typhoon Megi (2010) in the Northern South China Sea. *Journal of Geophysical Research: Oceans*, *119*(5), 3134–3157. <https://doi.org/10.1002/2013JC009661>
- Gutiérrez Brizuela, N., Alford, M. H., Xie, S.-P., Sprintall, J., Voet, G., Warner, S. J., et al. (2023). Prolonged thermocline warming by near-inertial internal waves in the wakes of tropical cyclones. *Down to Earth*. <https://doi.org/10.31223/X5NS9N>
- Hamann, M. M., Alford, M. H., Lucas, A. J., Waterhouse, A. F., & Voet, G. (2021). Turbulence driven by reflected internal tides in a supercritical submarine canyon. *Journal of Physical Oceanography*, *51*(2), 591–609. <https://doi.org/10.1175/JPO-D-20-0123.1>
- Hautala, S. L., Reid, J. L., & Bray, N. (1996). The distribution and mixing of Pacific water masses in the Indonesian Seas. *Journal of Geophysical Research*, *101*(C5), 12375–12389. <https://doi.org/10.1029/96JC00037>
- Hlyviak, J., & Nolan, D. S. (2019). The influence of oceanic barrier layers on tropical cyclone intensity as determined through idealized, coupled numerical simulations. *Journal of Physical Oceanography*, *49*(7), 1723–1745. <https://doi.org/10.1175/JPO-D-18-0267.1>
- Huang, P., Sanford, T. B., & Imberger, J. (2009). Heat and turbulent kinetic energy budgets for surface layer cooling induced by the passage of Hurricane Frances (2004). *Journal of Geophysical Research*, *114*(C12), C12023. <https://doi.org/10.1029/2009JC005603>
- Huffman, G. J., Bolvin, D. T., Braithwaite, D., Hsu, K., Joyce, R., Xie, P., & Yoo, S.-H. (2015). NASA global precipitation measurement (GPM) integrated multi-satellite retrievals for GPM (IMERG). *Algorithm Theoretical Basis Document (ATBD) Version, 4*, (p. 26).
- Hughes, K. G., Moum, J. N., & Shroyer, E. L. (2020). Evolution of the velocity structure in the diurnal warm layer. *Journal of Physical Oceanography*, *50*(3), 615–631. <https://doi.org/10.1175/JPO-D-19-0207.1>
- Jacob, S. D., Shay, L. K., Mariano, A. J., & Black, P. G. (2000). The 3D oceanic mixed layer response to Hurricane Gilbert. *Journal of Physical Oceanography*, *30*(6), 1407–1429. [https://doi.org/10.1175/1520-0485\(2000\)030<1407:TOMLRT>2.0.CO;2](https://doi.org/10.1175/1520-0485(2000)030<1407:TOMLRT>2.0.CO;2)
- Jansen, M. F., Ferrari, R., & Mooring, T. A. (2010). Seasonal versus permanent thermocline warming by tropical cyclones. *Geophysical Research Letters*, *37*(3). <https://doi.org/10.1029/2009GL041808>
- Johnson, H. L., & Garrett, C. (2004). Effects of noise on Thorpe scales and run lengths. *Journal of Physical Oceanography*, *34*(11), 2359–2372. <https://doi.org/10.1175/JPO3021.1>
- Johnston, T. M. S., Chaudhuri, D., Mathur, M., Rudnick, D. L., Sengupta, D., Simmons, H. L., et al. (2016). Decay mechanisms of near-inertial mixed layer oscillations in the Bay of Bengal. *Oceanography*, *29*(2), 180–191. <https://doi.org/10.5670/oceanog.2016.50>
- Johnston, T. M. S., & Rudnick, D. (2021). Float trajectory and CTD data [Dataset]. NASA. Retrieved from <https://www-air.larc.nasa.gov/cgi-bin/ArcView/camp2ex?TRAJECTORY=1JOHNSTON.SHAUN/>
- Johnston, T. M. S., & Rudnick, D. L. (2009). Observations of the transition layer. *Journal of Physical Oceanography*, *39*(3), 780–797. <https://doi.org/10.1175/2008JPO3824.1>
- Johnston, T. M. S., Rudnick, D. L., Brizuela, N., & Moum, J. N. (2020). Advection by the North Equatorial Current of a cold wake due to multiple typhoons in the Western Pacific: Measurements from a profiling float array. *Journal of Geophysical Research: Oceans*, *125*(4), e2019JC015534. <https://doi.org/10.1029/2019JC015534>
- Johnston, T. M. S., Wang, S., Lee, C.-Y., Moum, J. N., Rudnick, D. L., & Sobel, A. (2021). Near-inertial wave propagation in the wake of Super Typhoon Mangkhut: Measurements from a profiling float array. *Journal of Geophysical Research: Oceans*, *126*(2), e2020JC016749. <https://doi.org/10.1029/2020JC016749>
- Joint Typhoon Warning Center. (2022). Western North Pacific Ocean best track data. [Dataset]. U.S. Navy. Retrieved from <https://www.metoc.navy.mil/jtwc/jtwc.html?western-pacific>
- Jourdain, N. C., Lengaigne, M., Vialard, J., Madec, G., Menkès, C. E., Vincent, E. M., et al. (2013). Observation-based estimates of surface cooling inhibition by heavy rainfall under tropical cyclones. *Journal of Physical Oceanography*, *43*(1), 205–221. <https://doi.org/10.1175/JPO-D-12-085.1>
- Korty, R. L., Emanuel, K. A., & Scott, J. R. (2008). Tropical cyclone-induced upper-ocean mixing and climate: Application to equable climates. *Journal of Climate*, *21*(4), 638–654. <https://doi.org/10.1175/2007JCLI1659.1>
- Kundu, P. K., & Thomson, R. E. (1985). Inertial oscillations due to a moving front. *Journal of Physical Oceanography*, *15*(8), 1076–1084. [https://doi.org/10.1175/1520-0485\(1985\)015<1076:IODTAM>2.0.CO;2](https://doi.org/10.1175/1520-0485(1985)015<1076:IODTAM>2.0.CO;2)
- Kunze, E. (1985). Near-inertial wave propagation in geostrophic shear. *Journal of Physical Oceanography*, *15*(5), 544–565. [https://doi.org/10.1175/1520-0485\(1985\)015<0544:NIWPIG>2.0.CO;2](https://doi.org/10.1175/1520-0485(1985)015<0544:NIWPIG>2.0.CO;2)
- Kunze, E., & Sanford, T. (1984). Observations of near-inertial waves in a front. *Journal of Physical Oceanography*, *14*(3), 566–581. [https://doi.org/10.1175/1520-0485\(1984\)014%3C0566:OONIWI%3E2.0.CO;2](https://doi.org/10.1175/1520-0485(1984)014%3C0566:OONIWI%3E2.0.CO;2)
- Le Traon, P., Nadal, F., & Ducet, N. (1998). An improved mapping method of multisatellite altimeter data. *Journal of Atmospheric and Oceanic Technology*, *15*(2), 522–534. [https://doi.org/10.1175/1520-0426\(1998\)015<0522:AIMMOM>2.0.CO;2](https://doi.org/10.1175/1520-0426(1998)015<0522:AIMMOM>2.0.CO;2)
- Mater, B. D., Venayagamoorthy, S. K., St. Laurent, L., & Moum, J. N. (2015). Biases in Thorpe-scale estimates of turbulence dissipation. Part I: Assessments from large-scale overturns in oceanographic data. *Journal of Physical Oceanography*, *45*(10), 2497–2521. <https://doi.org/10.1175/JPO-D-14-0128.1>

- Mei, W., Primeau, F., McWilliams, J. C., & Pasquero, C. (2013). Sea surface height evidence for long-term warming effects of tropical cyclones on the ocean. *Proceedings of the National Academy of Sciences*, *110*(38), 15207–15210. <https://doi.org/10.1073/pnas.1306753110>
- Menkes, C. E., Lengaigne, M., Lévy, M., Ethé, C., Bopp, L., Aumont, O., et al. (2016). Global impact of tropical cyclones on primary production. *Global Biogeochemical Cycles*, *30*(5), 767–786. <https://doi.org/10.1002/2015GB005214>
- Moum, J., Farmer, D., Smyth, W., Armi, L., & Vagle, S. (2003). Structure and generation of turbulence at interfaces strained by internal solitary waves propagating shoreward over the continental shelf. *Journal of Physical Oceanography*, *33*(10), 2093–2112. [https://doi.org/10.1175/1520-0485\(2003\)033<2093:SAGOTA>2.0.CO;2](https://doi.org/10.1175/1520-0485(2003)033<2093:SAGOTA>2.0.CO;2)
- Nagai, T., Tandon, A., Kunze, E., & Mahadevan, A. (2015). Spontaneous generation of near-inertial waves by the Kuroshio Front. *Journal of Physical Oceanography*, *45*(9), 2381–2406. <https://doi.org/10.1175/JPO-D-14-0086.1>
- Névir, P., & Sommer, M. (2009). Energy–vorticity theory of ideal fluid mechanics. *Journal of the Atmospheric Sciences*, *66*(7), 2073–2084. <https://doi.org/10.1175/2008JAS2897.1>
- Nilsson, J. (1995). Energy flux from traveling hurricanes to the oceanic internal wave field. *Journal of Physical Oceanography*, *25*(4), 558–573. [https://doi.org/10.1175/1520-0485\(1995\)025<0558:EFFTHT>2.0.CO;2](https://doi.org/10.1175/1520-0485(1995)025<0558:EFFTHT>2.0.CO;2)
- Osborn, T. (1980). Estimates of the local rate of vertical diffusion from dissipation measurements. *Journal of Physical Oceanography*, *10*(1), 83–89. [https://doi.org/10.1175/1520-0485\(1980\)010<0083:EOTLRO>2.0.CO;2](https://doi.org/10.1175/1520-0485(1980)010<0083:EOTLRO>2.0.CO;2)
- Pollard, R. T., & Millard, R. (1970). Comparison between observed and simulated wind-generated inertial oscillations. *Deep-Sea Research and Oceanographic Abstracts*, *17*(4), 813–821. [https://doi.org/10.1016/0011-7471\(70\)90043-4](https://doi.org/10.1016/0011-7471(70)90043-4)
- Pollard, R. T., Rhines, P. B., & Thompson, R. O. (1973). The deepening of the wind-mixed layer. *Geophysical Fluid Dynamics*, *4*(4), 381–404. <https://doi.org/10.1080/03091927208236105>
- Price, J. F. (1981). Upper ocean response to a hurricane. *Journal of Physical Oceanography*, *11*(2), 153–175. [https://doi.org/10.1175/1520-0485\(1981\)011<0153:UORTAH>2.0.CO;2](https://doi.org/10.1175/1520-0485(1981)011<0153:UORTAH>2.0.CO;2)
- Price, J. F. (1983). Internal wave wake of a moving storm. Part I. Scales, energy budget and observations. *Journal of Physical Oceanography*, *13*(6), 949–965. [https://doi.org/10.1175/1520-0485\(1983\)013<0949:IWVOAM>2.0.CO;2](https://doi.org/10.1175/1520-0485(1983)013<0949:IWVOAM>2.0.CO;2)
- Price, J. F., Sanford, T. B., & Forristall, G. Z. (1994). Forced stage response to a moving hurricane. *Journal of Physical Oceanography*, *24*(2), 233–260. [https://doi.org/10.1175/1520-0485\(1994\)024<0233:FSRTAM>2.0.CO;2](https://doi.org/10.1175/1520-0485(1994)024<0233:FSRTAM>2.0.CO;2)
- Reul, N., Chapron, B., Grodsky, S. A., Guimbard, S., Kudryavtsev, V., Foltz, G. R., & Balaguru, K. (2021). Satellite observations of the sea surface salinity response to tropical cyclones. *Geophysical Research Letters*, *48*(1), e2020GL091478. <https://doi.org/10.1029/2020GL091478>
- Rudzin, J. E., Shay, L. K., & Jaimes de la Cruz, B. (2019). The impact of the Amazon–Orinoco River plume on enthalpy flux and air–sea interaction within Caribbean Sea tropical cyclones. *Monthly Weather Review*, *147*(3), 931–950. <https://doi.org/10.1175/MWR-D-18-0295.1>
- Salmon, R. (2007). A general method for conserving energy and potential enstrophy in shallow-water models. *Journal of the Atmospheric Sciences*, *64*(2), 515–531. <https://doi.org/10.1175/JAS3837.1>
- Sanabia, E. R., & Jayne, S. R. (2020). Ocean observations under two major hurricanes: Evolution of the response across the storm wakes. *AGU Advances*, *1*(3), e2019AV000161. <https://doi.org/10.1029/2019AV000161>
- Sanford, T. B., Ma, B. B., & Alford, M. H. (2021). Stalling and dissipation of a near-inertial wave (NIW) in an anticyclonic ocean eddy: Direct determination of group velocity and comparison with theory. *Journal of Geophysical Research: Oceans*, *126*(5), e2020JC016742. <https://doi.org/10.1029/2020JC016742>
- Schade, L. R., & Emanuel, K. A. (1999). The ocean’s effect on the intensity of tropical cyclones: Results from a simple coupled atmosphere–ocean model. *Journal of the Atmospheric Sciences*, *56*(4), 642–651. [https://doi.org/10.1175/1520-0469\(1999\)056<0642:TOSEOT>2.0.CO;2](https://doi.org/10.1175/1520-0469(1999)056<0642:TOSEOT>2.0.CO;2)
- Scotti, A. (2015). Biases in Thorpe-scale estimates of turbulence dissipation. Part II: Energetics arguments and turbulence simulations. *Journal of Physical Oceanography*, *45*(10), 2522–2543. <https://doi.org/10.1175/JPO-D-14-0092.1>
- Shay, L. K., & Chang, S. W. (1997). Free surface effects on the near-inertial ocean current response to a hurricane: A revisit. *Journal of Physical Oceanography*, *27*(1), 23–39. [https://doi.org/10.1175/1520-0485\(1997\)027<0023:FSEOTN>2.0.CO;2](https://doi.org/10.1175/1520-0485(1997)027<0023:FSEOTN>2.0.CO;2)
- Shay, L. K., Elsberry, R. L., & Black, P. G. (1989). Vertical structure of the ocean current response to a hurricane. *Journal of Physical Oceanography*, *19*(5), 649–669. [https://doi.org/10.1175/1520-0485\(1989\)019<0649:VSOTOC>2.0.CO;2](https://doi.org/10.1175/1520-0485(1989)019<0649:VSOTOC>2.0.CO;2)
- Shay, L. K., Mariano, A. J., Jacob, S. D., & Ryan, E. H. (1998). Mean and near-inertial ocean current response to Hurricane Gilbert. *Journal of Physical Oceanography*, *28*(5), 858–889. [https://doi.org/10.1175/1520-0485\(1998\)028<0858:MANIOC>2.0.CO;2](https://doi.org/10.1175/1520-0485(1998)028<0858:MANIOC>2.0.CO;2)
- Skamarock, W. C., Klemp, J. B., Dudhia, J., Gill, D. O., Barker, D. M., Wang, W., & Powers, J. G. (2008). *A description of the Advanced Research WRF version 3*. NCAR Technical note-475+ STR.
- Smyth, W., Zavialov, P., & Moum, J. (1997). Decay of turbulence in the upper ocean following sudden isolation from surface forcing. *Journal of Physical Oceanography*, *27*(5), 810–822. [https://doi.org/10.1175/1520-0485\(1997\)027<0810:DOTITU>2.0.CO;2](https://doi.org/10.1175/1520-0485(1997)027<0810:DOTITU>2.0.CO;2)
- Srifer, R. L., & Huber, M. (2007). Observational evidence for an ocean heat pump induced by tropical cyclones. *Nature*, *447*(7144), 577–580. <https://doi.org/10.1038/nature05785>
- Thomas, L. N., Rainville, L., Asselin, O., Young, W. R., Girton, J., Whalen, C. B., et al. (2020). Direct observations of near-inertial wave  $\zeta$ -refraction in a dipole vortex. *Geophysical Research Letters*, *47*(21), e2020GL090375. <https://doi.org/10.1029/2020GL090375>
- Thompson, A., Gille, S. T., MacKinnon, J. A., & Sprintall, J. (2007). Spatial and temporal patterns of small-scale mixing in Drake Passage. *Journal of Physical Oceanography*, *37*(3), 572–592. <https://doi.org/10.1175/JPO3021.1>
- Thompson, E. J., Moum, J. N., Fairall, C. W., & Rutledge, S. A. (2019). Wind limits on rain layers and diurnal warm layers. *Journal of Geophysical Research: Oceans*, *124*(2), 897–924. <https://doi.org/10.1029/2018JC014130>
- Thorpe, S. (1977). Turbulence and mixing in a Scottish loch. *Philosophical Transactions of the Royal Society of London - Series A: Mathematical and Physical Sciences*, *286*(1334), 125–181. <https://doi.org/10.1098/rsta.1977.0112>
- Turner, J., & Kraus, E. (1967). A one-dimensional model of the seasonal thermocline I. A laboratory experiment and its interpretation. *Tellus*, *19*(1), 88–97. <https://doi.org/10.1111/j.2153-3490.1967.tb01461.x>
- Vincent, E. M., Lengaigne, M., Madec, G., Vialard, J., Samson, G., Jourdain, N. C., et al. (2012). Processes setting the characteristics of sea surface cooling induced by tropical cyclones. *Journal of Geophysical Research*, *117*(C2). <https://doi.org/10.1029/2011JC007396>
- Wallcraft, A., Metzger, E., & Carroll, S. (2009). *Software design description for the hybrid coordinate ocean model (HYCOM), Version 2.2 (Tech. Rep.)*. Naval Research Lan Stennis Space Center MS Oceanography Div.
- Walsh, K., Fiorino, M., Landsea, C., & McInnes, K. (2007). Objectively determined resolution-dependent threshold criteria for the detection of tropical cyclones in climate models and reanalyses. *Journal of Climate*, *20*(10), 2307–2314. <https://doi.org/10.1175/JCL14074.1>
- Wamsley, L. (2018). *Dozens more feared dead in the Philippines after typhoon triggers mudslide*. National Public Radio. Retrieved from <https://www.npr.org/2018/09/17/648866035/dozens-more-feared-dead-in-the-philippines-after-typhoon-triggers-mudslide>
- Wang, S. (2020). Mixed layer velocity and surface wind stress from numerical simulation of Super Typhoon Mangkhut [Dataset]. Zenodo. <https://doi.org/10.5281/zenodo.4134671>

- Whitt, D. B., & Thomas, L. N. (2015). Resonant generation and energetics of wind-forced near-inertial motions in a geostrophic flow. *Journal of Physical Oceanography*, 45(1), 181–208. <https://doi.org/10.1175/JPO-D-14-0168.1>
- Yablonsky, R. M., & Ginis, I. (2009). Limitation of one-dimensional ocean models for coupled hurricane–ocean model forecasts. *Monthly Weather Review*, 137(12), 4410–4419. <https://doi.org/10.1175/2009MWR2863.1>
- Zhang, H., Wu, R., Chen, D., Liu, X., He, H., Tang, Y., et al. (2018). Net modulation of upper ocean thermal structure by typhoon Kalmaegi (2014). *Journal of Geophysical Research: Oceans*, 123(10), 7154–7171. <https://doi.org/10.1029/2018JC014119>
- Zweers, N., Makin, V., De Vries, J., & Burgers, G. (2010). A sea drag relation for hurricane wind speeds. *Geophysical Research Letters*, 37(21). <https://doi.org/10.1029/2010GL045002>